Robo4 contributes to the turnover of Peyer's patch B cells

MSc Ruth Fair-Mäkelä[1], PhD Milas Ugur[2]*, PhD Imtiaz Iftakhar-E-Khuda[1]*, MSc Laura Kähäri[1], PhD Anu Kukkonen-Macchi[1], Heini-Maria Brenyah[1], MD, PhD Kati Elima[1], MD, PhD Masayuki Miyasaka[1], PhD Oliver Pabst[2] and MD, PhD Sirpa Jalkanen[1]

[1]MediCity Research Laboratory and Institute of Biomedicine, University of Turku, 20520 Turku, Finland

[2]Institute of Molecular Medicine, RWTH Aachen University, 52074 Aachen, Germany

*These authors contributed equally to the work

Correspondence: Sirpa Jalkanen, Medicity Research Laboratory, University of Turku, Tykistökatu 6 A, FIN-20520 Turku, Finland. Tel: +358-29-4504379

E-mail: sirpa.jalkanen@utu.fi

The authors declare no competing interests.

Acknowledgments

We thank Heidi Gerke, Riikka Sjöroos, Riina Mankonen, Sari Mäki and Etta-Liisa Väänänen for technical help, as well as Marko Salmi for the supervision and financial support of H.-M.B. We acknowledge the Cell Imaging Core at the Turku Centre for Biotechnology. This work was supported by the Finnish Academy, the Finnish Cancer Foundation, the Sigrid Juselius Foundation, and a grant by the Deutsche Forschungsgemeinschaft DFG PA921/3-1. This work benefited from data assembled by the ImmGen consortium.

Key words: lymphatics, Peyer's patches, B cell turnover

Abstract

All leukocytes can get entrance into the draining lymph nodes via the afferent lymphatics but only lymphoid cells can leave the nodes. The molecular mechanisms behind this phenomenon have remained unknown. We employed genome wide microarray analyses of the subcapsular sinus and lymphatic sinus (LS) endothelial cells and found Robo4 to be selectively expressed on LS lymphatics. Further analyses showed high Robo4 expression in lymphatic vessels of Peyer's patches, which only have efferent lymphatic vessels. In functional assays, Robo4 deficient animals showed accumulation of naive B cells ($CD19^{+}/CD62L^{hi}/CD44^{lo}$) in Peyer's patches, whereas no difference was seen within other lymphocyte subtypes. Short-term lymphocyte homing via high endothelial venules to peripheral and mesenteric lymph nodes and Peyer's patches was also slightly impaired in Robo4 knockout animals. These results show for the first time, selective expression of Robo4 in the efferent arm of the lymphatics and its role in controlling the turnover of a subset of B lymphocytes from Peyer's patches.

Introduction

Lymphocytes recirculate continuously between the blood and lymphatic organs[1]. Most lymphocytes enter the lymphoid organs via the high endothelial venules. Molecular mechanisms and different phases in lymphocyte-blood vessel endothelial cell interactions during the lymphocyte extravasation have been extensively studied during the last 30 years and are currently well known[2, 3, 4, 5]. In contrast, cell trafficking via the lymphatics is much less characterized although it is a central functional part of our immune system and a route for cancer cells to metastasize. Certain lymphocytes, dendritic cells and other leukocytes together with antigens enter the lymph nodes via afferent lymphatic vessels, which drain to the subcapsular sinus (SS) of the lymph nodes. In physiological conditions only lymphoid cells, however, can exit the nodes via the efferent lymphatic sinuses[6, 7, 8]. The exit routes for lymphoid cells go via chains of lymph nodes[9]. For example, cells leaving the popliteal lymph nodes go next to sacral and further to iliac lymph nodes and cells leaving the Peyer's patches (PP) go to the mesenteric lymph nodes (MLN)[10, 11]. Although discriminative trafficking between the afferent and efferent arms is a well-known phenomenon, its molecular basis has remained largely unknown.

We have characterized the afferent and efferent lymphatic endothelial cells of the lymph nodes and found a multitude of molecular differences between these different arms of the lymphatic system[12]. One of the differently expressed molecules was magic roundabout, i.e. Robo4, a member of the Roundabout axon guidance family[12]. The microarray data can be found at www.ncbi.nlm.nih.gov/geo (accession no. GSE68371). Robo4 was first characterized on blood endothelium[13], although it is also expressed on hematopoietic stem cells in the bone marrow. It determines their

location in the bone marrow niches and regulates directional trafficking of the stem cells[14, 15]. On blood endothelium Robo4 contributes to endothelial cell integrity as well as to permeability and inhibits pathologic angiogenesis by antagonizing the function of VEGF[16]. Robo4 has been reported to interact with UNC5B and Slit2, although there has been some debate about the role of Slit2 as a ligand of Robo4[17, 18, 19]. Slit2 was found to inhibit lipopolysaccharide-induced secretion of certain inflammatory mediators and monocyte adhesion to the endothelium in a Robo4-mediated fashion suggesting the importance of the Slit2-Robo4 pathway in regulating the state of the endothelium at sites of inflammation[20].

The role of Robo4 on lymphatics is poorly known. To date, it has only been studied by using lymphatic endothelial cells *in vitro*. Slit2 inhibited VEGF-C induced proliferation, migration and tube formation of lymphatic endothelial cells (LEC) *in vitro* and the effect was Robo4 dependent[21]. In this present study, we found selective expression of Robo4 in the efferent arm of the lymphatics and explored its possible role in lymphocyte turnover in the peripheral and mucosal nodes. The results indicate a new function for Robo4: it controls turnover of a B cell subpopulation in PP.

Results

Robo4 is preferentially expressed on the efferent arm of the lymphatics

Genome wide microarray analyses were performed using RNA from isolated LECs of murine subcapsular sinus (SS) and lymphatic sinuses (LS) using the laser capture micro dissection method and cell sorting with flow cytometry[12]. The purpose was to identify differentially expressed genes between the afferent and efferent arms of the lymphatic vasculature in the lymph nodes. In combined analyses, Robo4 had a 13.1-fold higher expression in LS than in SS (www.ncbi.nlm.nih.gov/geo (accession no. GSE68371)). Expression of Robo4 on lymphatics as such was in agreement with the ImmGen data regarding Robo4 expression in blood and lymphatic vessel endothelial cells (http://www.immgen.org/databrowser/, Fig. 1a, b), and therefore, we wanted to analyse its role in the lymphatics more closely. It turned out that none of the tested antibodies (commercial and available) worked in immunohistochemical stainings in mouse, but did so in immunofluorescence stainings of cell suspensions followed by FACS analyses. To check whether Robo4 is present on the efferent lymphatics, we first stained lineage$^-$, CD45$^-$/podoplanin$^+$/LYVE1$^+$ cells from peripheral and mesenteric lymph nodes (PLN and MLN pooled) (Fig. 1c). To analyse Robo4 expression in immunohistochemical stainings, we produced a monoclonal anti-murine Robo4 antibody by taking advantage of Robo4 KO animals (Fig. S1a-e). To detect Robo4 in the lymph node we administered the Robo4 antibody subcutaneously (s.c.) into the footpads of C57BL/6 mice to harness the draining lymphatics to deliver the antibody to its targets in the draining lymph node. Non-specific binding of the antibody to macrophage Fc receptors was blocked using Fc receptor blocking antibodies and mouse immunoglobulins administered before and with the anti-Robo4 antibody[22].

Robo4 expression was detected mainly in the efferent lymphatics in the medullary region (Fig. 1d, Fig. S2a, b). Very faint Robo4 expression was also visible in the LYVE1$^-$ LECs of the subcapsular sinus roof, whereas the LYVE1$^+$ floor seemed to be negative for Robo4 (Fig. 1d). According to the observations by Kähäri et al.[22], s.c. injected antibodies do not reach the luminal side of blood vessels, which may well explain why we were not able to detect vascular Robo4 after s.c. injection of the antibody (Fig. 1d). Expression of Robo4 was particularly high and homogenous in LECs isolated from PP Fig. 1e, f). This observation is consistent with the lack of afferent lymphatics in PP. Thus, LECs within PP might mostly resemble efferent lymphatics and consistently express Robo4. Moreover, we tested Robo4 expression on lymphatics leading from the gut to the MLN (Fig. 1e). Expression of Robo4 on LYVE1$^+$ LEC was higher in the close vicinity to the gut than on lymphatic vessels further away leading to the MLN, which become afferent vessels for MLN by definition (Fig. 1g, h).

Heterogeneous expression of Robo4 was seen in LECs of PLN and MLN. Only a subpopulation was as highly positive as in PP while the rest of the LEC were practically negative (Fig. 1c). Similarly, we stained skin lymphatics, which all are afferent lymphatics by definition. Very little staining was seen in these cells (Fig. 1i).

Robo4 on human efferent lymphatics supports lymphocyte binding

Next, we tested whether the expression of human Robo4 resembles that of mouse. Also in human lymph nodes collected from the head and neck region, Robo4 was expressed on a subset of LS endothelial cells and it was absent from the lymphatic endothelium in SS (Fig. 2a, b). We used the appendix as an organized human mucosal lymphoid tissue in the expression analyses. A subpopulation of Prox-1 positive

lymphatics in human appendix was Robo4 positive (Fig. 2c). To explore a possible role of human Robo4 on the LS endothelium, we performed *ex vivo* frozen section-binding assays. In this assay, lymphocytes bind specifically to the lymphatic endothelium in the SS and LS (and to high endothelial venules, HEV, which are easy to discriminate from the lymphatic endothelium by their plump morphology).[12, 23] Anti-Robo4 antibody significantly inhibited lymphocyte binding to the lymphatic endothelium in the LS but not in the SS (Fig. 2d, Fig. S3a-d) suggesting that Robo4 on the lymphatic endothelium of LS directly interacts with lymphocytes.

The major lymphocyte pools and lymphatic architecture is normal in Robo4 knockout mice

Next, we took advantage of Robo4 KO mice and studied their lymphocyte pools and lymphatic and blood vasculature in PP. Special emphasis was put on the PP, because of the abundant Robo4 expression on their lymphatics. The major lymphocyte pools (B220, CD4, and CD8) did not differ statistically significantly and they showed comparable anatomic localization in PP (Fig. 3a-d). Numbers of CD4 and CD8 cells were lower in PLN of KO mice than in their controls but such a difference was not observed in MLN (Fig. S4a-d).

Despite the suggested role of Robo4 in angiogenesis and lymphangiogenesis, the lymphatic and blood vasculature analysed by using anti-LYVE1, anti-MAdCAM-1 and anti-CD31 antibodies was normal based on the area the vessels covered and their microscopical appearance. Data regarding PP are shown in Fig. 3e-h.

Robo4 contributes to lymphocyte entrance to PP

As Robo4 is abundantly present on blood endothelium, we first checked its possible contribution to lymphocyte entrance into the lymph nodes via HEV. We adoptively transferred congenic $CD45.1^+$ lymphocytes into Robo4 KO and WT animals and analysed them from PP, PLN, MLN and peripheral blood 2 and 18 hours after the i.v. injections. There was a slight decrease at the 2-hour time point in the homing of all $CD45.1^+$ and $CD45.1^+ CD4^+$ cells to the PP of Robo4 KO mice in comparison to their WT controls (Fig. 4a). In contrast, no differences at the 18-hour time point were seen (Fig. 4b, the gating strategy is shown in Fig. S5a-d) suggesting a statistically significant contribution for Robo4 in lymphocyte homing via HEV to PP at early time points. A concomitant increase in the number of transferred cells in peripheral blood of KO mice was observed (Fig. 4c). We also checked the homing of $CD45.1^+$ lymphocytes to PLN and MLN and observed a quantitatively minor, although statistically significant decrease in the homing of different lymphocyte subpopulations to these organs in Robo4 KO mice in comparison to their WT controls (Fig. S5e-h). There were no significant anatomical differences in the distribution of transferred cells between the KO and WT mice in PP (Fig. 4d, e) or PLN and MLN (Fig. S6a-d).

Robo4 is involved in B cell turnover in PP

To study the turnover of endogenous lymphocytes FITC was injected into PPs. In this model, FITC will label the lymphocytes and the kinetics of the turnover can simply be analysed by measuring the number of different FITC positive lymphocyte subsets retaining in PPs after 24 hours. These studies showed that more $CD19^+$ and especially $CD62^{hi}CD44^{lo}$ B cells were left in the PPs of Robo4 KO than in those of WT mice

suggesting a Robo4 dependent mechanism regulating B cell turnover in PP (Fig. 5a, b). There was no difference in the number of T cell subtypes suggesting a clearly specific contribution of Robo4 towards the B cell turnover. There was also a trend towards an impaired exit of lymphocytes from popliteal lymph nodes to iliac lymph nodes after lymphocyte transfer to footpads (Fig. S7a, b). We then performed qPCR analyses of PP B cells to discover possible changes in selected molecules known to be involved in lymphocyte exit and maybe indirectly affected by lack of Robo4 on lymphatics or imprinting during the development as hematopoietic stem cells express Robo4. PP B cells had significantly less S1P receptor 1 signal most likely contributing to the impaired turnover of B cells from the PP (Fig. S8a-c). We next checked how well $CD19^{+}CD62L^{hi}CD44^{lo}$ B cells enter PP in adoptive transfer assays. The results clearly showed that the entrance of this B cell subpopulation was normal in Robo4 KO mice (Fig. 5c). In the immunohistological analyses, $CD19^{+}CD62L^{hi}CD44^{lo}$ B cells are mainly located in the mantle zone of germinal centers in PP (Fig. 5d) and can be mainly classified as naïve based on their IgD positivity (Fig. 5e). When analysing the $CD62L^{hi}CD44^{lo}$ population of total $CD19^{+}$ B cells in the FITC-injection experiments (Fig. 5a, b), no differences were found between KO and WT animals (Fig. 5f) suggesting a slower turnover for that population in the KO animals. We also employed thorough endogenous B cell subtype analyses of PP and bone marrow and found that the mean values of naïve and germinal center B cells in PP were higher in the KO mice. This, however, showed only a trend in statistical analyses (Fig. 5g-n). Similarly, the numbers of B cell progenitors in bone marrows were comparable between Robo4 KO and their controls (Fig. S9a-e) as were the numbers of B cell subpopulations in MLN expect for regulatory B cells, the number of which were higher in KO mice (Fig. S9f-i).

Robo4 KO have slightly increased apoptosis in PP

As the KO mice retain CD19 positive B cells in PP in excess without any difference in their entrance two possibilities remain; the PPs have more apoptosis regulating the increasing cell amount over time or they enlarge over time in Robo4 KO mice. We tested these two possibilities. To study the rate of apoptosis we analysed Robo4 KO and WT PP lymphocytes by staining them for Annexin V that binds to externally exposed phosphatidylserine on the cell membrane. We analysed the early apoptotic Annexin V^+ population in total $CD45^+$ hematopoietic cells, $B220^+$ B cells and $CD3^+$ T cells (Fig. 6a-c) and discovered that Robo4 KO mice have a slight increase in the total cell number of $CD45^+$ Annexin V^+ early apoptotic cells. The late stage of apoptosis was measured with the TUNEL assay detecting cells with fragmented DNA from Robo4 KO and WT PP frozen sections (Fig. 6d, e). In these stainings, the TUNEL assay revealed a comparable number and localization of the apoptotic cells in the whole PP and the follicle regions in Robo4 KO mice and their WT controls. Our data suggests that Robo4 KO mice have a slightly activated rate of apoptosis among $B220^+$ B cells that may keep the size of PP under control.

Imbalance in MLN homeostasis leads to increased tissue size

While Robo4 KO PP were not enlarged when their tissue weight was normalized to the weight of the animal, MLN of Robo4 KO mice had a greater mass when compared to their WT controls at ages of 12 weeks or more (Fig. 7a,b). To study what would cause the increased growth of MLN in these mice, we examined the size of different B cell populations (Fig. 7c, d). The percentage of $CD19^+CD62L^-CD44^+$ population was slightly increased in Robo4 KO MLN (Fig. 7d). $CD19^+CD62L^{hi}CD44^{lo}$ B cells localized in the

mantle zone of B cell follicles similar to PP (Fig. 7e). However, an increase in one B cell population does not explain the clear increase in tissue weight. Therefore, we examined the total percentage and number of $CD19^+$ B cells, which was not altered in Robo4 KO MLN (Fig. 7f). There was no increase in the total $CD45^+$ hematopoietic cells in Robo4 KO MLN either (Fig. 7g). To study the apoptotic rate, we stained MLN lymphocytes with Annexin V and quantified the early apoptotic cells as well as the dead cells in Robo4 KO MLN. Although the rate of early apoptotic cells was comparable in Robo4 KO and WT MLN, a clear increase in the dead cell population in $CD45^+$ cells, $B220^+$ B cells and $CD3^+$ T cells was found (Fig. 7h, i). This was accompanied by increased collagen I deposits (Fig. 7j).

Discussion

The function of Robo4 as a regulator of angiogenesis, endothelial cell migration and blood vascular integrity has been demonstrated[16, 18, 24]. In contrast, very little is known regarding its expression and function in the lymphatics. In this work, we found Robo4 to be preferentially expressed on the efferent arm of the lymphatic system. The finding was further confirmed by the presence of Robo4 in the lymphatics of PP, which are by definition efferent in their nature as PP do not have any afferent lymphatics. However, when approaching the mesenteric lymph nodes the PP draining lymphatics lose Robo4 expression – a finding that is compatible with the fact that these same vessels become afferent for the mesenteric lymph nodes. The expression pattern of Robo4 in these different arms of the lymphatics opposes the expression of macrophage scavenger receptor, which is discriminatively expressed on afferent lymphatics while being absent on the efferent ones[12].

Although the diverse roles of Robo4 on blood endothelium presented above have been demonstrated, its possible role in leukocyte trafficking via HEV in organized lymphoid tissues has not been addressed. About 80% of the lymphocytes are thought to enter the lymph nodes via HEV while 20% enter via the afferent lymphatics[25]. To be able to address the role of Robo4 in the trafficking dynamics of recirculating lymphocytes, we first studied whether Robo4 on HEVs contributes to lymphocyte entrance into the nodes. The results of these assays suggest that Robo4 does have a minor contribution to the entrance of certain lymphocyte subpopulations via the blood vessels into the PLN, MLN and PP, but the B cell homing via HEV to PP is at the same level both in Robo4 KO and their WT controls. Therefore, it is unlikely that the entry via HEV would contribute to the impaired turnover of the B cells by any means.

Originally, we performed genome wide screening of endothelial cells isolated from afferent and efferent lymphatics, because we were interested in finding molecules discriminatively expressed on the afferent and efferent arms of the lymphatic vasculature[12]. In addition, we were searching for potential candidates that would be responsible either for the leukocyte entry into the nodes or for selective lymphocyte access into the efferent lymphatics while leaving the nodes. Therefore, Robo4 seemed to be a good candidate in this respect. In functional assays, we utilized Robo4 KO mice and injected FITC locally into the PP. The results showed that a subset of endogenous B cells accumulate and thus, may have difficulties in leaving PP while CD4 and CD8 cells leave normally. We also detected significantly lower levels of S1P receptor 1 in PP B cells in Robo4 KO mice than in those of their WT controls. How can Robo4 have an effect on this? One possibility is imprinting during early developmental

296 phases as Robo4 is expressed by hematopoietic stem cells. Alternatively, lack of Robo4
297 from lymphatics indirectly affects the exit machinery of the lymphocytes.

298 *Ex vivo* adhesion assays measuring lymphocyte binding to HEV in frozen
299 sections was originally presented by Stamper and Woodruff[26]. Since then, several
300 modifications have been employed including measurements of leukocyte and tumor
301 cell binding to different types of lymphatic vessels[23, 27, 28]. Importantly this method has
302 shown its usability for the molecular identification of several interaction partners both
303 on leukocytes and vascular walls[29, 30]. Many of the molecules functionally
304 characterized this way have been later used as targets in drug development[31, 32, 33].
305 We also utilized this method to test, whether anti-Robo4 antibody is able to inhibit
306 lymphocyte binding to lymphatics in human lymph nodes. The results of these assays
307 unambiguously demonstrated that lymphocyte-lymphatic endothelial cell interaction
308 in the LS but not in the SS is Robo4 dependent being in agreement with the expression
309 pattern of Robo4.

310 In conclusion, we have for the first time demonstrated the discriminative
311 expression of Robo4 in the efferent arm of the lymphatic vasculature and its role in
312 regulating the composition of B cell populations in PP. This may happen at least
313 partially by adhesive interactions between B cells and endothelial cells within LS.
314 Robo4 differs from CXCR4, Clever-1 and sphingosine 1 phosphate, which contribute to
315 lymphocyte egress from PP but are also involved in lymphocyte trafficking in the
316 afferent arm of the lymphatics[34, 35, 36]. This finding is expected to facilitate future
317 studies regarding the possibilities to target Robo4 and thus, manipulate the immune
318 response.

319

Materials and methods

Mice

C57BL/6 mice were purchased from Jackson Laboratory and Janvier labs. Robo4 KO mice, 129S6(B6)-*Robo4*^{tm1Lex}/Mmucd (stock number 032543-UCD) and their wild-type controls from the same genetic background were purchased from Lexicon genetics Inc. Mice were bred as separate Robo4 KO and WT lines. Congenic CD45.1^{+} B6.SJL-*Ptprc*^{a} *Pepc*^{b}/BoyJ mice were purchased from Jackson Laboratory (stock number 002014). Age and sex matched controls were used for the study. Robo4 KO mice have originally been subjected to a broad phenotypic screen aiming at identifying defects in metabolism, function of the cardiovascular, neurological or immunological systems as well as involvement in oncogenesis, but no notable phenotype alterations were found[37]. All animal experiments were approved by the Ethical Committee for Animal Experimentation in Finland and Germany. Experiments were performed according to the rules and regulations of The Finnish Act on Animal Experimentation (497/2013) in compliance with the 3R-principle with the appropriate animal licenses (5587/04.10.07/2014, 5762/04.10.07/2017 and 84-02.04.2014.A330).

Human material

Human lymph nodes and appendix samples were obtained from surplus tissues from surgical operations. Tissues were carefully examined macroscopically and microscopically before using tissues for experiments. Only tissues that were observed as normal were used for further experimentation. Mononuclear cells were isolated from healthy volunteers with the permission of the Ethical Committee of the Turku University Hospital.

Antibodies

The antibodies used in this work are listed in Supplementary Table 1.

Flow cytometry

When analyzing lymphocytes, single-cell suspensions were prepared by homogenizing PLN, MLN and PP with custom-made metal cell strainers or nylon filters followed by additional filtering. Lymphatic endothelial cells were isolated as described previously[12]. Cells were blocked using the anti-CD16/CD32 Mouse BD Fc Block™ (BD 553141) or 5% rat serum before staining the cells with appropriate combinations of fluorescently labeled monoclonal antibodies. Cells were analyzed with an LSR II or LSR Fortessa cytometer (Becton Dickinson) that were appropriately calibrated for each antibody cocktail using UltraComp eBeads™ Compensation beads (Invitrogen™, 01-2222-41). Data was analysed using FlowJo software (FlowJo LLC).

Subcutaneous administration of anti-Robo4 antibody

In-house produced monoclonal anti-Robo4 antibody (see Supplementary methods) was conjugated using the Alexa Fluor™ 647 Protein Labelling Kit (Invitrogen™, A20173). Before injections, the antibody was filtered using a 10-kDa cut-off centrifugal filter unit (Millipore, MRCPRT010) to remove any free fluorochromes. A blocking mixture targeted to block the Fc receptors present on macrophages was a combination of 50 µg anti-CD16/CD32 (clone 2.4G2, Bio X Cell BE0307) and 50 µg mouse immunoglobulins (Rockland 010-0102-0005). 20 µl of the blocking mixture was administered to the footpads of C57BL/6 mice, which were under light isoflurane anesthesia. The blocking antibodies and immunoglobulins were let to drain to the

popliteal lymph node for 15 minutes. 5 µg of Anti-Robo4 antibody (clone FuRFM7) was injected simultaneously with 50 µg of anti-CD16/CD32 and 50 µg of mouse Ig s.c. to the calves of the mice and antibodies were let to drain to the popliteal lymph node for an additional 15 min after which the mice were sacrificed, the lymph nodes excised, embedded in optimal cutting temperature (OCT) in a predetermined orientation in order to produce transverse sections of the lymph node and snap-frozen using dry ice. The samples were stored at -70 °C and 6 µm sections were cut for imaging. The lymph node tissue sections were subjected to immunofluorescence staining of vascular and lymphatic markers CD31-A488 (BioLegend®, 102514) and LYVE1 (ReliaTech GmbH, 103-PA50) followed by a conjugated secondary antibody, Goat anti-rabbit Alexa Fluor® 546 (Invitrogen™, A11035). Samples were imaged using a LSM780 confocal microscope (Carl Zeiss) as described below.

Immunohistochemistry

Processing tissues for microscopy. Harvesting and treating PP for imaging was performed as previously described[34]. Upon harvesting PP no external pressure was applied to the tissue in order to preserve the lymphatic contents. PP were harvested attached to a ring of the intestine that was flushed with PBS to empty the intestinal contents. The PP were fixed in 4% PFA for 2-4 hours, washed twice with PBS and incubated overnight in 30% sucrose. On the following day, PP were embedded in OCT compound in a predetermined position in order to produce transverse sections of the PP. Inguinal lymph nodes and the MLN were harvested and excess fat tissue was removed. LN were fixed in 4% PFA for 2-4 hours, incubated in 30% sucrose overnight and embedded in OCT on the following day. Blocks were snap-frozen using dry ice,

stored at -70 °C and used for cutting 6 µm sections. Tissue sections were subjected for immunofluorescence staining by incubating them with predetermined antibody dilutions for 30-60 min each at room temperature. Stained sections were mounted using ProLong™ Gold Antifade Mountant with DAPI (Invitrogen™, P36931) or without DAPI (Invitrogen™, P10144). In some cases, PP and MLN were embedded in OCT compound without PFA fixation and the sections were subsequently fixed with ice-cold acetone before staining.

Human lymph nodes and appendixes were collected from three different donors and they were embedded in OCT medium, snap-frozen with dry ice, stored at -70 °C and used for cutting 5 µm sections fixed with acetone. Non-specific binding sites were blocked with 5% human AB serum for 10 min at room temperature. Sections were stained with predetermined antibody dilutions for 30 min each at room temperature and mounted using ProLong™ Gold Antifade Mountant.

Imaging. The immunofluorescently stained sections were imaged using a LSM780 or LSM880 confocal microscopes (Carl Zeiss) with a Plan-Apochromat 20x/0.8 objective. Zen 2010 or Zen 2.3 SP1 FP2 software (Carl Zeiss) was used for acquiring images. The same slice thickness for each channel was determined by adjusting the pinhole resulting in a slice thickness varying from 2.3 µm to 8.8 µm. In some cases, images were acquired using an Olympus BX60 fluorescence microscope (Tokyo, Japan) equipped with a UPlanFI 20x/0.50 or an UPlanFI 40x/0.75 objective or a Nikon Eclipse TI-E fluorescence microscope and a Plan Apo lamda 20x/0.80 objective.

Image analyses were performed using ImageJ software (version 1.52i). Linear brightness adjustments were applied equally to Robo4 KO and WT images as well as

human tissue images and their controls. Image quantification was performed by thresholding the appropriate signal and calculating area fractions for the tissues. Thresholding was applied equally to all analyzed images. When analyzing collagen I, background subtraction was performed before thresholding. Adoptive transfer image quantifications were done by thresholding CD45.1$^+$ signal and calculating area fractions of determined regions of interest, such as follicular and interfollicular regions (PP) or CD19$^+$ B cell regions as well as CD4$^+$ T cell regions (MLN, PLN). MLN samples were analyzed from a representative area of 1.61-1.62 mm^2. Collagen I$^+$ signal was thresholded and the total area and percentage of collagen I$^+$ signal were analyzed from two representative 0.24 mm^2 areas/sample.

Apoptosis assay

Annexin V. To analyze the apoptotic rate and dead cells in Robo4 KO and WT tissues, we stained single-cell suspensions extracted from PP and MLN with Fixable Viability Dye eFluor 506 (eBioscience 65-0866-14) diluted in PBS for 30 min on ice. After washes, the cells were blocked with the anti-CD16/CD32 Mouse BD Fc Block™ and incubated with fluorescently conjugated antibodies for 30 min on ice as described above. After staining with antibodies, cells were washed with PBS and incubated with Annexin V-PE (BD 556422) diluted 1:200 in 1x Annexin staining buffer comprised of 0.01 M HEPES (pH 7.4), 0.14 M NaCl and 2.5 mM $CaCl_2$. The samples were incubated for 15 min at room temperature, additional Annexin-staining buffer was added to the cells and samples were acquired immediately using an LSR Fortessa cytometer (Becton Dickinson).

TUNEL. Robo4 KO and WT PP were harvested, fixed in 4% PFA for 4 h, washed with PBS twice and incubated overnight in 30% sucrose. PP were mounted the following day in OCT as described above. Frozen sections of 5-6 µm were cut and apoptotic cells were detected from Robo4 KO and WT PP using the commercially available Click-iT™ Plus TUNEL Assay (Invitrogen™, C10618) fluorescently detecting the 3'-OH ends of fragmented DNA. The assay was performed according to the manufacturer's instructions. The sections were subsequently subjected to antibody staining detecting B cells and lymphatics. TUNEL staining was quantified using ImageJ by thresholding the TUNEL$^+$ signal and calculating area fractions of the signal in relation to the whole PP or follicular areas.

Intravenous staining of PP HEV

Mucosal HEV were quantified using intravenous labeling of endothelial cells with anti-MAdCAM-1 antibody. For quantifying MAdCAM-1$^+$ HEVs in Robo4 KO and WT PP tissue sections, 10 µg of anti-MAdCAM-1 antibody (clone Meca367, a gift from Prof. E. Butcher) was administered to Robo4 KO and WT mice intravenously to label the lumens of HEVs. Mice were sacrificed 10 min later and the PP were harvested. Frozen sections were stained with the secondary antibody goat anti-rat IgG (H+L) Alexa Fluor 546 (Invitrogen™, A11081) detecting Meca367. The sections were simultaneously stained for CD31 and IgD.

Adoptive transfer assays

Lymphocytes were isolated from skin-draining, mesenteric and cervical lymph nodes of wild-type, congenic CD45.1$^+$ donor mice. Tissues were homogenized using metal

custom-made cell strainers to produce a single-cell suspension. 12 x10^6 CD45.1$^+$ lymphocytes were intravenously transferred into CD45.2$^+$ Robo4 KO and WT mice. PLN (inguinal, axillary, brachial), MLN, PP and peripheral blood of the recipient mice were analyzed 2 and 18 hours after the intravenous transfer.

In another set of experiments, lymphocytes were isolated from the spleens, skin-draining lymph nodes and cervical lymph nodes of Robo4 WT mice. Donor cells were labeled with 0.5 µM CellTrace™ CFSE (Invitrogen™, C34554) and 10 x10^6 cells were subcutaneously injected into the hind leg footpads of Robo4 KO and WT recipient mice. Popliteal and iliac lymph nodes were analyzed with flow cytometry 12 hours after the adoptive transfer.

FITC injection into PP

FITC injection into PP was done as previously described[38]. Briefly, mice were anesthetized and the small intestine was exposed after small incisions into the skin and peritoneum. FITC (Fluorescein isothiocyanate, Sigma-Aldrich) solution diluted in PBS at the concentration of 1 mg/ml was injected into 4-5 PP per mouse. For injections, fine glass capillaries connected to a microinjector (Harvard Apparatus) were used. After the injections, the small intestine was placed back into the abdominal cavity and the wounds were closed with sutures and metal clips. The mice were analyzed 1 day after the FITC injections with flow cytometry.

Ex vivo adhesion assays

In principle, the adhesion assays were performed as described earlier[23]. Briefly, human lymphocytes from healthy volunteers were isolated from peripheral blood using Ficoll-

Paque™ (GE Healthcare) density gradient purification. Isolated lymphocytes were incubated on freshly cut frozen sections of human peripheral lymph nodes pre-treated for 30 min with rabbit anti-human Robo4 antibody (ab10547, Abcam) or normal rabbit serum as a negative control. Lymphocytes were allowed to bind to the sinuses for 5 min in rotatory conditions, in steady state conditions for 15 min followed by 5 min in rotatory conditions and thereafter, 15 min without rotation at +7 °C. The non-bound cells were gently decanted off from the sections and adherent cells were fixed with 1% glutaraldehyde. The number of lymphocytes bound to the SS and LS was counted under dark-field microscopy. To be able to standardize day-to-day variations between the experiments, the binding of lymphocytes to the control sections was set to 100% by definition.

Statistical analyses

Sample size for experiments was determined with pilot assays. All numerical data are presented as mean ± S.D. Comparisons between the genotypes or differently treated groups were analyzed using the Mann-Whitney *U*-test or the two-tailed Student's t test. All statistical analyses were performed with GraphPad Prism v7 software (GraphPad software Inc.). Outliers in data were determined using the Grubb's test available from GraphPad Prism and removed from the analyses. *P*-values under 0.05 were considered as statistically significant.

Supplementary Material is linked to the online version of the paper at http://www.nature.com/mi.

Author contributions

These authors contributed equally: Milas Ugur and Imtiaz Iftakhar-E-Khuda. S. Jalkanen, R. Fair-Mäkelä, M. Miyasaka and O. Pabst designed the experiments. R. Fair-Mäkelä, M. Ugur, I. Iftakhar-E-Khuda, L. Kähäri, A. Kukkonen-Macchi and H.-M. Brenyah performed and analyzed the experiments. K. Elima collected the data. R. Fair-Mäkelä and S. Jalkanen wrote the first drafts and all authors contributed to the final version of the manuscript.

Competing interests

The authors declare no competing interests.

522 **References**

523 1. Gowans, J.L. & Knight, E.J. The route of re-circulation of lymphocytes in rat.
524 *Proc R Soc Lond B Biol Sci* **159**, 257-282 (1964).
525 2. Habtezion, A., Nguyen, L.P., Hadeiba, H. & Butcher, E.C. Leukocyte Trafficking
526 to the Small Intestine and Colon. *Gastroenterology* **150**, 340-354 (2016).
527 3. Miyasaka, M. & Tanaka, T. Lymphocyte trafficking across high endothelial
528 venules: dogmas and enigmas. *Nat Rev Immunol* **4**, 360-370 (2004).
529 4. Bevilacqua, M. *et al.* Selectins: a family of adhesion receptors. *Cell* **67**, 233
530 (1991).
531 5. McEver, R.P. Selectins: initiators of leucocyte adhesion and signalling at the
532 vascular wall. *Cardiovasc Res* **107**, 331-339 (2015).
533 6. Teijeira, A., Rouzaut, A. & Melero, I. Initial afferent lymphatic vessels
534 controlling outbound leukocyte traffic from skin to lymph nodes. *Front Immunol* **4**, 433
535 (2013).
536 7. Hunter, M.C., Teijeira, A. & Halin, C. T Cell Trafficking through Lymphatic
537 Vessels. *Front Immunol* **7**, 613 (2016).
538 8. Randolph, G.J., Ivanov, S., Zinselmeyer, B.H. & Scallan, J.P. The Lymphatic
539 System: Integral Roles in Immunity. *Annu Rev Immunol* **35**, 31-52 (2017).
540 9. Forster, R., Braun, A. & Worbs, T. Lymph node homing of T cells and dendritic
541 cells via afferent lymphatics. *Trends Immunol* **33**, 271-280 (2012).
542 10. Kawashima, Y., Sugimura, M., Hwang, Y-C. & Kudo, N. The lymph system in
543 mice. Japan J Vet Res 12:69-78 (1964).
544

11. Guy-Grand, D., Griscelli, C. & Vassalli, P. The gut-associated lymphoid system: nature and properties of the large dividing cells. *Eur J Immunol* **4**, 435-443 (1974).

12. Iftakhar, E.K.I. *et al.* Gene-expression profiling of different arms of lymphatic vasculature identifies candidates for manipulation of cell traffic. *Proc Natl Acad Sci USA* **113**, 10643-10648 (2016).

13. Huminiecki, L., Gorn, M., Suchting, S., Poulsom, R. & Bicknell, R. Magic roundabout is a new member of the roundabout receptor family that is endothelial specific and expressed at sites of active angiogenesis. *Genomics* **79**, 547-552 (2002).

14. Smith-Berdan, S. *et al.* Robo4 cooperates with CXCR4 to specify hematopoietic stem cell localization to bone marrow niches. *Cell Stem Cell* **8**, 72-83 (2011).

15. Smith-Berdan, S., Nguyen, A., Hong, M.A. & Forsberg, E.C. ROBO4-mediated vascular integrity regulates the directionality of hematopoietic stem cell trafficking. *Stem Cell Reports* **4**, 255-268 (2015).

16. Jones, C.A. *et al.* Robo4 stabilizes the vascular network by inhibiting pathologic angiogenesis and endothelial hyperpermeability. *Nat Med* **14**, 448-453 (2008).

17. Koch, A.W. *et al.* Robo4 maintains vessel integrity and inhibits angiogenesis by interacting with UNC5B. *Dev Cell* **20**, 33-46 (2011).

18. Park, K.W. *et al.* Robo4 is a vascular-specific receptor that inhibits endothelial migration. *Dev Biol* **261**, 251-267 (2003).

19. Zhang, B. *et al.* Repulsive axon guidance molecule Slit3 is a novel angiogenic factor. *Blood* **114**, 4300-4309 (2009).

20. Zhao, H., Anand, A.R. & Ganju, R.K. Slit2-Robo4 pathway modulates lipopolysaccharide-induced endothelial inflammation and its expression is dysregulated during endotoxemia. *J Immunol* **192**, 385-393 (2014).

21. Yu, J. *et al.* Slit2N and Robo4 regulate lymphangiogenesis through the VEGF-C/VEGFR-3 pathway. *Cell Commun Signal* **12**, 25 (2014).

22. Kähäri, L. *et al.* Transcytosis route mediates rapid delivery of intact antibodies to draining lymph nodes. *J Clin Invest* **129**, 3086-3102 (2019).

23. Irjala, H. *et al.* Mannose receptor is a novel ligand for L-selectin and mediates lymphocyte binding to lymphatic endothelium. *J Exp Med* **194**, 1033-1042 (2001).

24. Marlow, R. *et al.* Vascular Robo4 restricts proangiogenic VEGF signaling in breast. *Proc Natl Acad Sci U S A* **107**, 10520-10525 (2010).

25. Salmi, M. & Jalkanen, S. How do lymphocytes know where to go: current concepts and enigmas of lymphocyte homing. *Adv Immunol* **64**, 139-218 (1997).

26. Stamper, H.B., Jr. & Woodruff, J.J. Lymphocyte homing into lymph nodes: In vitro demonstration of the selective affinity of recirculating lymphocytes for high-endothelial venules. *J Exp Med* **144**, 828-833 (1976).

27. Jalkanen, S., Bargatze, R., Herron, L. & Butcher, E.C. Human lymphocyte-high endothelial venule interaction: functional and molecular characterization. *Adv Exp Med Biol* **186**, 615-620 (1985).

28. Irjala, H. *et al.* Mannose receptor (MR) and common lymphatic endothelial and vascular endothelial receptor (CLEVER)-1 direct the binding of cancer cells to the lymph vessel endothelium. *Cancer Res* **63**, 4671-4676 (2003).

29. Pals, S.T. *et al.* Evidence that leukocyte-function associated antigen-1 is involved in recirculation and homing of lymphocytes via high endothelial venules. *J Immunol* **140**, 1851-1853 (1988).

591 30. Streeter, P.R., Rouse, B.T.N. & Butcher, E.C. Immunohistologic and functional
592 characterization of a vascular addressin involved in lymphocyte homing into
593 peripheral lymph nodes. *J Cell Biol* **107**, 1853-1862 (1988).
594 31. Yednock, T.A. *et al.* Prevention of experimental autoimmune
595 encephalomyelitis by antibodies against a4b1 integrin. *Nature* **356**, 63-66 (1992).
596 32. Salmi, M. & Jalkanen, S. A 90-kilodalton endothelial cell molecule mediating
597 lymphocyte binding in humans. *Science* **257**, 1407-1409 (1992).
598 33. Irjala, H. *et al.* The same endothelial receptor controls lymphocyte traffic both
599 in vascular and lymphatic vessels. *Eur J Immunol* **33**, 815-824 (2003).
600 34. Schmidt, T.H., Bannard, O., Gray, E.E. & Cyster, J.G. CXCR4 promotes B cell
601 egress from Peyer's patches. *J Exp Med* **210**, 1099-1107 (2013).
602 35. Gohda, M. *et al.* Sphingosine 1-phosphate regulates the egress of IgA
603 plasmablasts from Peyer's patches for intestinal IgA responses. *J Immunol* **180**, 5335-
604 5343 (2008).
605 36. Geherin, S.A., Wilson, R.P., Jennrich, S. & Debes, G.F. CXCR4 is dispensable for
606 T cell egress from chronically inflamed skin via the afferent lymph. *PLoS One* **9**, e95626
607 (2014).
608 37. Tang, T. *et al.* A mouse knockout library for secreted and transmembrane
609 proteins. *Nat Biotechnol* **28**, 749-755 (2010).
610 38. Schulz, O. *et al.* Hypertrophy of infected Peyer's patches arises from global,
611 interferon-receptor, and CD69-independent shutdown of lymphocyte egress. *Mucosal*
612 *Immunol* **7**, 892-904 (2014).
613

614 **Figure legends**

615

616 **Fig. 1** Robo4 is expressed on lymphatic and blood vessel endothelium. **a, b** Expression
617 of *Robo4* mRNA in peripheral lymph nodes (PLN, **a**) or mesenteric lymph node (MLN,
618 **b**) of wild-type C57BL/6J mice. mRNA expression was detected from lymphatic
619 endothelial cells ($CD45^-$, $CD31^+$, $Podoplanin^+$, LEC) and blood endothelial cells ($CD45^-$,
620 $CD31^+$, $Podoplanin^-$, BEC). Data are from the Immunological genome project, mean
621 values above 120 (dashed red line) are regarded as positive with 95% confidence. **c**
622 Robo4 protein expression is detected in WT BEC and LEC. The cells were isolated and
623 pooled from PLN and MLN. **d** Immunostaining of popliteal lymph node after
624 subcutaneous (s.c.) administration of Robo4-A647 antibody and *ex vivo* staining of
625 CD31 and LYVE1 to detect the BEC and LEC cell populations. Scale bars 200 µm, 50 µm
626 zoom-ins, n=3. **e** A schematic drawing of gut lymph nodes and lymphatics showing the
627 PP, the efferent lymphatics leading from the lamina propria and PP to the MLN, arrows
628 point to the areas analyzed for Robo4 expression in **f-h.** Robo4 protein expression was
629 analyzed with flow cytometry from BEC, LEC, $LYVE1^+$ LEC and $LYVE1^-$ LEC isolated from
630 PP (**f**), the gut-lining region (**g**) and connecting lymphatics between the gut and MLN
631 (**h**). **i** Robo4 expression in skin LEC. Black histograms, Robo4; grey histograms, isotype
632 specific control. Flow cytometry in **c** and **f-i** n=3. Data are presented as mean ± S.D.
633 $***P < 0.001$, $**P < 0.01$ (two-tailed Student's t-test). M, medulla, SS, subcapsular
634 sinus.

635

636 **Fig. 2** Robo4 is expressed in human efferent lymphatics where it mediates binding of
637 lymphocytes to the lymphatic sinus. **a, b** Low power images of immunostaining of

Robo4 and Clever-1 (a lymphatic endothelial marker) in human lymph nodes (**a**). In the close-up images (**b**) the arrowhead indicates Robo4$^+$ Clever-1$^-$ blood vessel in the capsule, open arrows point to Robo4$^-$ Clever-1$^{-/lo}$ roof of SS and closed arrows indicate the Robo4$^-$ Clever-1$^+$ floor of SS; Robo4$^+$ Clever-1$^+$ lymphatics are only present in LS. **c** Immunostaining of Robo4 and Prox1 in the human appendix. Arrows indicate Robo4$^+$ Prox1$^+$ lymphatic staining. Negative control stainings for Robo4 are shown in the boxed areas. Representatives of 3 lymph nodes and 3 appendix samples from different individuals (scale bars 50 µm). **d** Adhesion of peripheral blood lymphocytes to lymph node frozen sections (n=12) analysed by *ex vivo* adhesion assays of three different individuals. The sections were treated with anti-Robo4 or an isotype control antibody and adhered lymphocytes were enumerated manually from the subcapsular and lymphatic sinuses. Data is shown as the adhesion of lymphocytes to anti-Robo4 treated samples in relation to their isotype controls. The control values were set as 100 by definition. Data are presented as mean ± S.D. ****P* < 0.001 (two-tailed Student's t-test). C, capsule, SS, subcapsular sinus, LS, lymphatic sinus.

Fig. 3 Robo4 KO mice have a normal number and distribution of lymphocytes and endothelial cells in PP. Frequency (**a**) and number (**b**) of B cells (B220$^+$), CD4$^+$ and CD8$^+$ T cells in the total lymphocyte pool in Robo4 KO and WT PP assessed by flow cytometry. Data are pooled from two independent experiments with 8-9 WT and 9 Robo4 KO mice. **c-h** Immunostainings and quantifications of Robo4 KO and WT PP showing distribution of lymphocyte subpopulations (**c, d**), LYVE1$^+$ lymphatics (**e, h**), MAdCAM-1$^+$ HEV detected with a secondary antibody after i.v. injections of Meca367 antibody (**f, h**) or CD31$^+$ blood vessels (**g, h**). Images were quantified from 3-4 WT and

3 Robo4 KO mice from 1-2 individual PP per mouse and 1-3 sections per PP, scale bars 200 µm. Data are presented as mean ± S.D. Each dot represents an individual mouse (**a, b**) or an analysed sample (**c-h**).

Fig. 4 Vascular Robo4 regulates short-term lymphocyte migration to Peyer's patches. **a-b** Relative number of adoptively transferred CD45.1$^+$ total lymphocytes, CD19$^+$ CD45.1$^+$ B cells, CD4$^+$ CD45.1$^+$ and CD8$^+$ CD45.1$^+$ T cells recovered in PP with flow cytometry 2 hours (**a**) or 18 hours (**b**) after intravenous injections of donor cells into Robo4 KO and WT recipients. **c** Relative amount of adoptively transferred CD45.1$^+$ lymphocytes recovered from peripheral blood with flow cytometry 2 hours (top) or 18 hours (bottom) after intravenous injections of donor cells into Robo4 KO and WT recipients. In **a-c** data are pooled from three independent 2-hour and two independent 18-hour adoptive transfer assays with 15-17 Robo4 KO and 15-18 WT (2-hour) or 12-13 Robo4 KO and 9-11 WT mice (18-hour). The mean value of WT mice is defined as 1.0. **d-e** The distribution of adoptively transferred CD45.1$^+$ cells was analysed from PP frozen sections and the percentage (%) of CD45.1$^+$ cells was quantified from CD19$^+$ B cell follicles (**d**) or CD19$^-$ inter-follicular regions (**e**) at 2 hours (top) or 18 hours (bottom) after intravenous injections based on the signal area covered by CD45.1$^+$ cells/total area analysed. Image quantification was performed from 1-2 independent 2-hour and 18-hour experiments analysing 3-9 Robo4 KO and WT mice. Sections were analysed from a total of 8-12 (**d**) or 4-10 (**e**) PP. Representative images are shown from the 18-hour adoptive transfer experiment (scale bars=100 µm). Data are presented as mean ± S.D. $*P < 0.05$, $**P < 0.01$, $***P < 0.001$ (Mann-

685 Whitney *U*-test). Each dot represents an individual mouse (**a-c**) or an analysed sample
686 (**d-e**). F, follicle, I, inter-follicular region.
687
688 **Fig. 5** Robo4 KO mice retain especially $CD19^{+}CD62L^{hi}CD44^{lo}$ B cells in their PP. **a**
689 Representative plots showing frequencies of $FITC^{+}CD62L^{hi}CD44^{lo}$cells among $CD19^{+}$
690 cells in FITC injected PP 24 hours post injections. **b** Frequency of $FITC^{+}$
691 $CD19^{+}CD62L^{hi}CD44^{lo}$ B cells (left), $CD4^{+}CD62L^{hi}CD44^{lo}$ T cells (middle) and
692 $CD8^{+}CD62L^{hi}CD44^{lo}$ T cells (right) recovered by flow cytometry from FITC injected
693 Robo4 KO and WT PP 24 hours after FITC injections. Combined data are pooled from
694 three individual experiments performed with 6 WT and 6 KO mice per group. **c** Relative
695 number of adoptively transferred naïve $CD19^{+}CD62L^{hi}CD44^{lo}$ $CD45.1^{+}$ B cells recovered
696 from Robo4 KO and WT PP with flow cytometry 18 hours after intravenous injections
697 of $CD45.1^{+}$ donor cells into Robo4 KO and WT recipients. Data are from 7 WT and 5 KO
698 mice. **d** Localization of $CD19^{+}CD62L^{hi}CD44^{lo}$ B cells. Arrows point to clusters of these
699 cells (scale bars 200 µm in main images, 20 µm in zoom-ins), n=3 WT and 3 KO mice.
700 **e** Gating of the $CD19^{+}CD62^{hi}CD44^{lo}$ population of B cells for the analysis of IgD
701 positivity (naïve B cells). **f** Frequency (%) of the $CD62L^{hi}CD44^{lo}$ population of total
702 $CD19^{+}$ B cells in the experiments described in **a** and **b**. **g-n** Analysis of endogenous B
703 cell populations in Robo4 KO and WT PP. Gating strategy and quantification of naïve B
704 cells ($B220^{+}$ IgD^{+}; **g, h**), activated B cells ($B220^{+}$ $CD19^{+}$ $CD40^{+}$ $MHCII^{+}$, **i, j**), germinal
705 center B cells ($B220^{+}$ IgD^{lo} $CD95^{+}$ $GL7^{+}$, **k, l**) and regulatory B cells ($CD19^{+}$ $CD1d^{+}$ $CD5^{+}$,
706 **m, n**). The percentage (%) of B cell subpopulations was normalized to $B220^{+}$ B cells
707 (left graph) and the number of B cell subpopulations is reported in relation to mg of
708 tissue (right graph). Endogenous B cells were quantified from two independent

709 experiments using 9 WT and 9 KO mice. Each dot represents and individual PP (**b, f**) or
710 an individual mouse (**c, h, j, l, n**). Data are presented as mean ± SD. *** $P < 0.001$
711 (Mann-Whitney *U*-test). T, T cell area, GC, germinal center.
712
713 **Fig. 6** Robo4 KO mice have slightly increased apoptosis in PP. **a-c** Early apoptotic cells
714 in Robo4 KO and WT PP. Frequency (%) and total cell numbers in relation to mg of
715 tissue of early apoptotic Annexin$^+$ CD45$^+$ cells (**a**), Annexin$^+$ B220$^+$ B cells (**b**) and
716 Annexin$^+$ CD3$^+$ T cells (**c**) analysed from Robo4 KO and WT PP. Apoptotic cells were
717 quantified from two independent experiments using 8-9 WT and 9-10 KO mice. **d**
718 Representative images from Robo4 KO and WT PP showing end-phase apoptotic cells
719 detected with TUNEL assay, B220$^+$ B cells and LYVE1$^+$ lymphatics (scale bars 200 µm in
720 main images, 100 µm in zoom-ins). **e** Quantification of the percentage (%) of TUNEL$^+$
721 area in Robo4 KO and WT PP analysed from the whole PP area (top) of follicle area
722 (bottom). Quantification of TUNEL$^+$ signal was performed from 6 WT and 5 KO PP
723 isolated from 3 WT and 3 KO mice. F, follicle. Data are presented as mean ± S.D. * $P <$
724 0.05 (Mann-Whitney *U*-test).
725
726
727 **Fig. 7** Differences in cell death and collagen homeostasis lead to increased MLN size
728 in Robo4 KO mice. **a, b** Weight of single PP (**a**) and MLN (**b**) in relation to the total
729 weight of the mouse analysed from Robo4 KO and WT mice under the age of 12 weeks
730 or 12 weeks and older. Tissues were weighed from 27 WT and 27 KO (<12 weeks), 20-
731 26 WT and 17-23 KO (>12 weeks) mice. **c, d** Gating and analysis of CD19$^+$ B cell
732 subpopulations from >12 weeks old mice. **c** FACS plots of CD19$^+$ subpopulations from

Robo4 KO and WT MLN analysed from >12 week old mice. **d** Frequency (%) and total cell numbers in relation to mg of tissue for $CD19^+CD62L^{hi}CD44^{lo}$ (left), $CD19^+CD62L^{hi}CD44^+$ (middle) and $CD19^+CD62L^-CD44^+$ (right) B cells recovered by flow cytometry of MLN of Robo4 KO and WT mice, age >12 weeks. Data are representative of two independent experiments performed with a total of 11-12 WT and KO mice. **e** Localization of $CD19^+CD62L^{hi}CD44^{lo}$ B cells in MLN of Robo4 KO and WT detected by immunostaining, age >12 weeks. Arrows point to these cells (scale bars 100 µm in main images, 20 µm in zoom-ins). **f, g** Frequency (%) and total cell numbers in relation to mg of tissue of $CD19^+$ B cells (**f**) and $CD45^+$ cells (**g**) analysed by flow cytometry from Robo4 KO and WT MLN, age >12 weeks. Data are pooled from two independent experiments with 11 WT and 12 KO mice. **h, i** Frequency (%) and total cell numbers in relation to mg of tissue of early apoptotic $Annexin^+$ $CD45^+$ cells, $Annexin^+$ $B220^+$ B cells, and $Annexin^+$ $CD3^+$ T cells (**h**) as well as dead $CD45^+$, dead $B220^+$ and dead $CD3^+$ cells (**i**) analysed from Robo4 KO and WT MLN, age >12 weeks. 5-6 WT and 6 KO mice were analysed. **j** Quantification of collagen I from fluorescence images of Robo4 KO and WT MLNs, age >12 weeks. Examples of the collagen I expression (left), combined results of the expression (right). Images were acquired from 6 WT and 6 KO mice and collagen I was quantified from two regions of 0.24 mm^2 for each MLN, scale bars 100 µm. Each dot represents an individual mouse (**a, b, d, f, g, h, i**) or an analysed sample (**j**). Data are presented as mean ± S.D. * $P < 0.05$, ** $P < 0.01$, *** $P < 0.001$ (Mann-Whitney *U*-test).

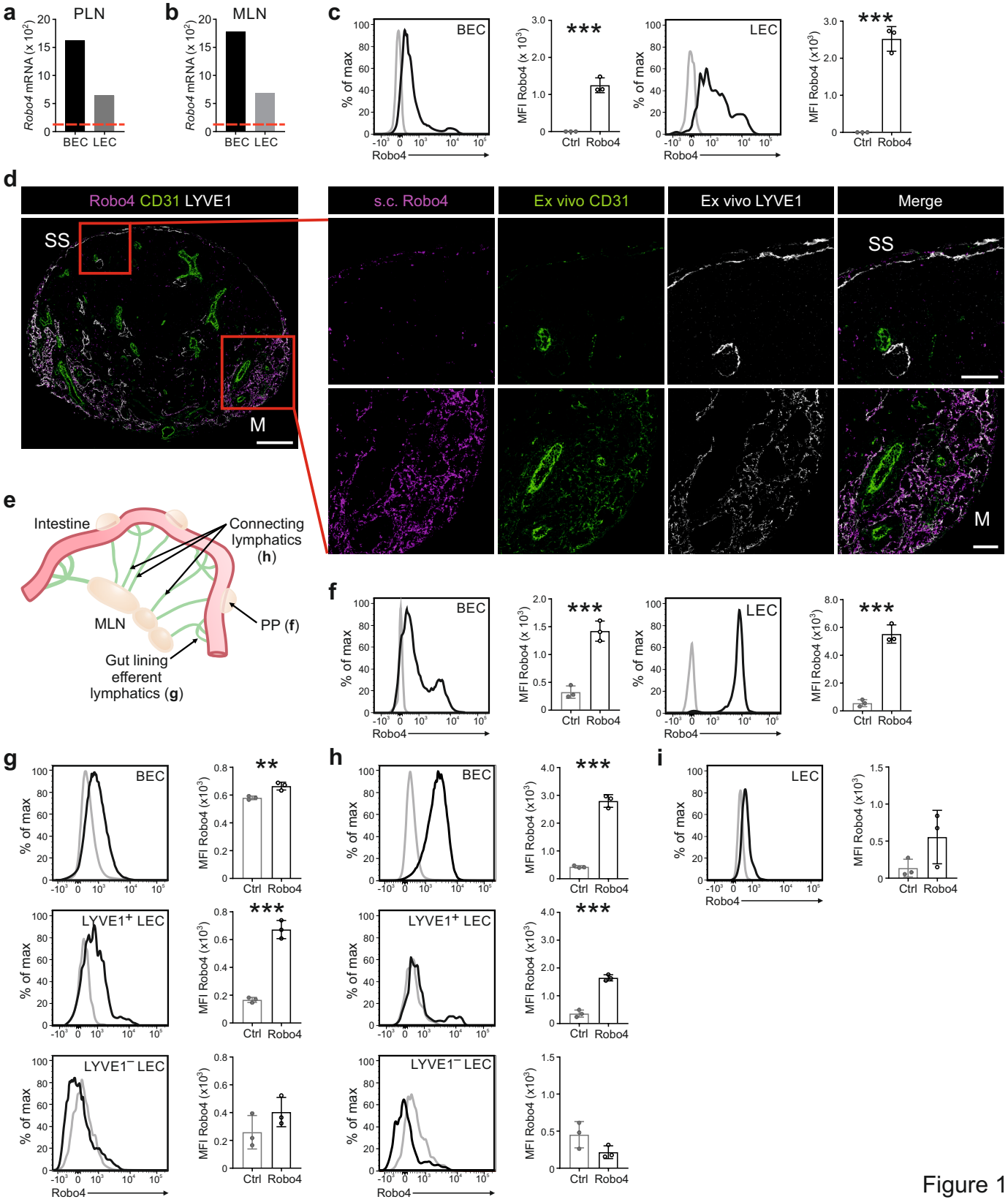
a
PLN
Robo4 mRNA (x 10²)
BEC LEC
b
MLN
Robo4 mRNA (x 10²)
BEC LEC
c
BEC
% of max
Robo4
MFI Robo4 (x 10³)
***
Ctrl Robo4
LEC
% of max
Robo4
MFI Robo4 (x10³)
***
Ctrl Robo4
d
Robo4 CD31 LYVE1
SS
M
s.c. Robo4
Ex vivo CD31
Ex vivo LYVE1
Merge
SS
M
e
Intestine
Connecting lymphatics (h)
MLN
PP (f)
Gut lining efferent lymphatics (g)
f
BEC
% of max
Robo4
MFI Robo4 (x 10³)
***
Ctrl Robo4
LEC
% of max
Robo4
MFI Robo4 (x10³)
***
Ctrl Robo4
g
BEC
% of max
MFI Robo4 (x10³)
**
Ctrl Robo4
LYVE1⁺ LEC
% of max
MFI Robo4 (x10³)
***
Ctrl Robo4
LYVE1⁻ LEC
% of max
Robo4
MFI Robo4 (x10³)
Ctrl Robo4
h
BEC
% of max
MFI Robo4 (x10³)
***
Ctrl Robo4
LYVE1⁺ LEC
% of max
MFI Robo4 (x10³)
***
Ctrl Robo4
LYVE1⁻ LEC
% of max
Robo4
MFI Robo4 (x10³)
Ctrl Robo4
i
LEC
% of max
Robo4
MFI Robo4 (x10³)
Ctrl Robo4

Figure 1

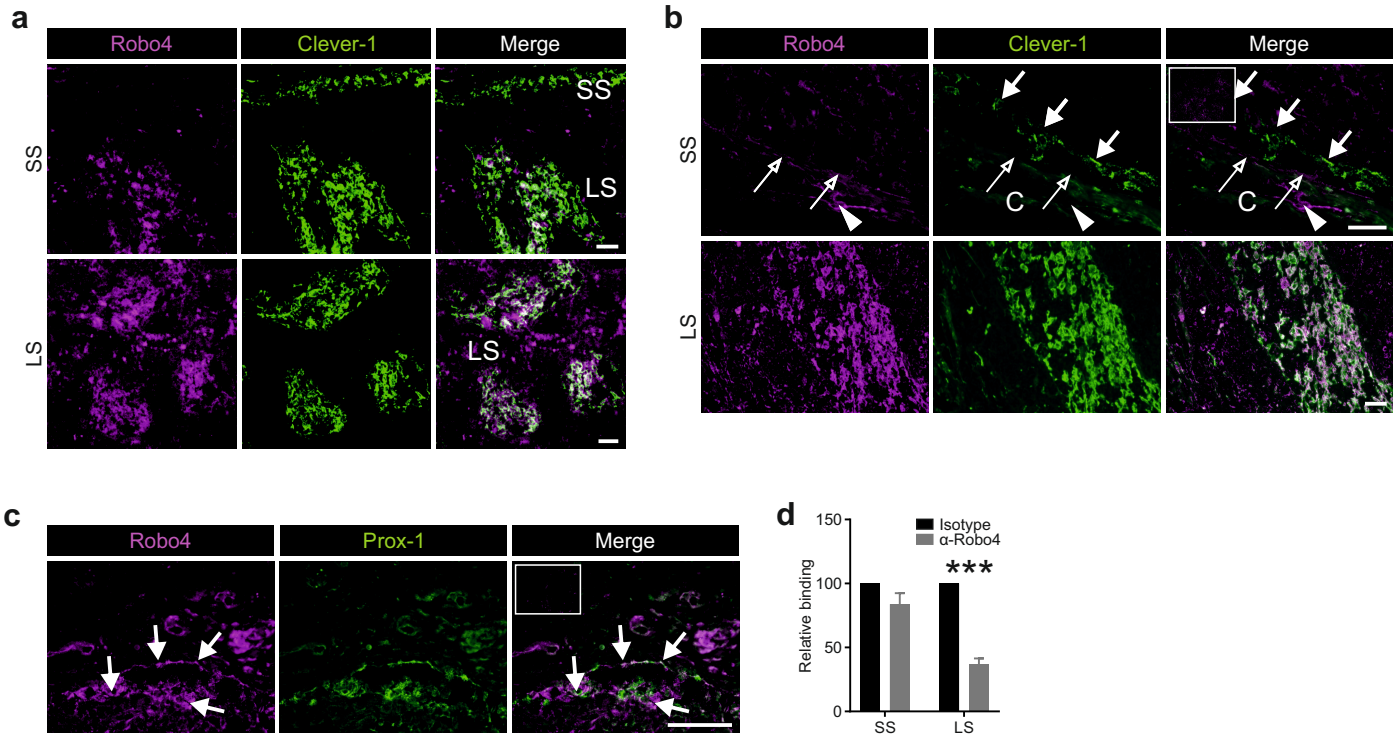
a
Robo4
Clever-1
Merge
SS
LS
SS
LS
LS
b
Robo4
Clever-1
Merge
SS
LS
C
C
c
Robo4
Prox-1
Merge
d
Isotype
α-Robo4
***
Relative binding
150
100
50
0
SS
LS

Figure 2

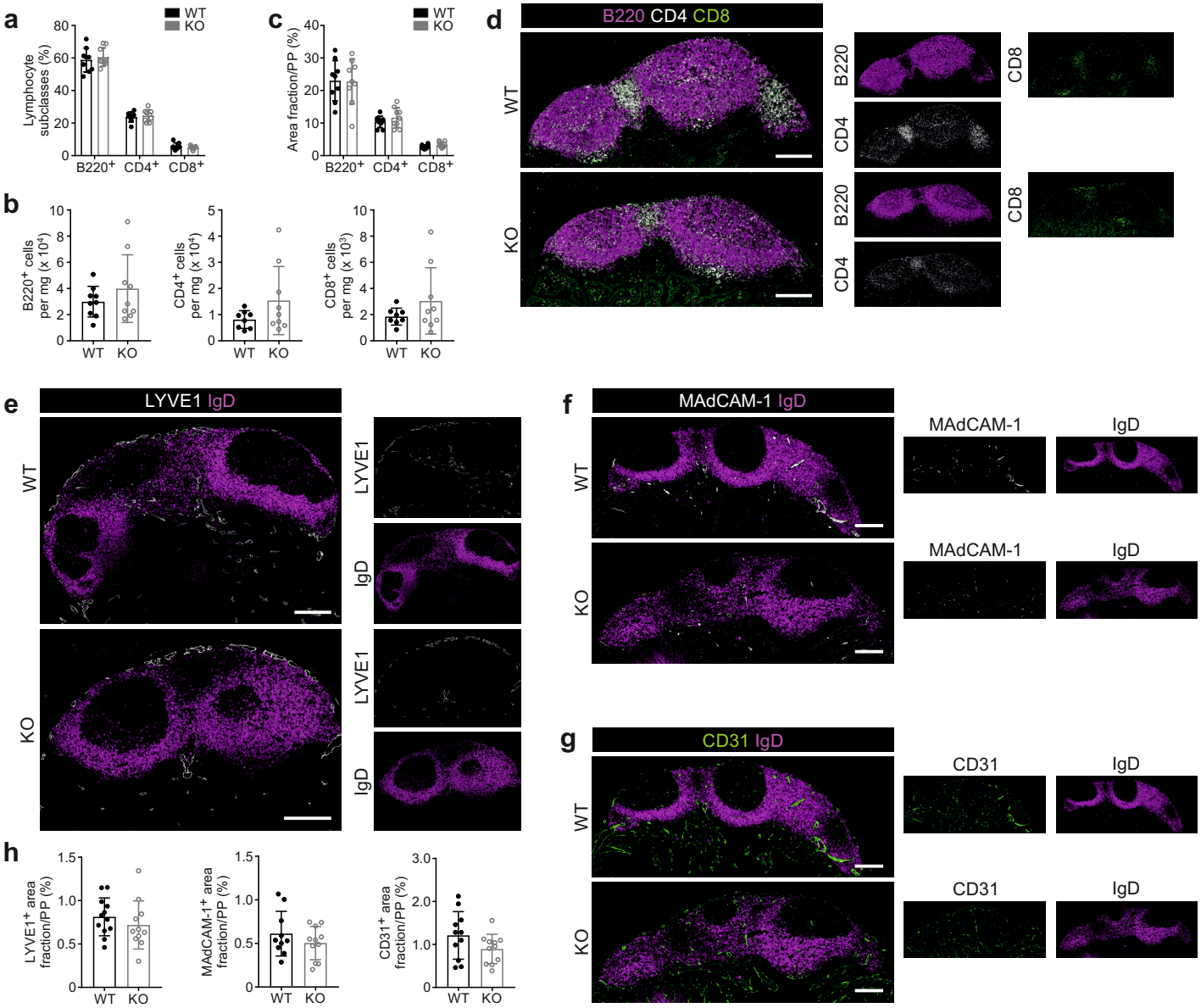
a
WT
KO
Lymphocyte subclasses (%)
B220+ CD4+ CD8+
c
Area fraction/PP (%)
b
B220+ cells per mg (x 10^4)
CD4+ cells per mg (x 10^4)
CD8+ cells per mg (x 10^3)
d
B220 CD4 CD8
B220
CD4
CD8
e
LYVE1 IgD
LYVE1
IgD
f
MAdCAM-1 IgD
MAdCAM-1
g
CD31 IgD
CD31
h
LYVE1+ area fraction/PP (%)
MAdCAM-1+ area fraction/PP (%)
CD31+ area fraction/PP (%)

Figure 3

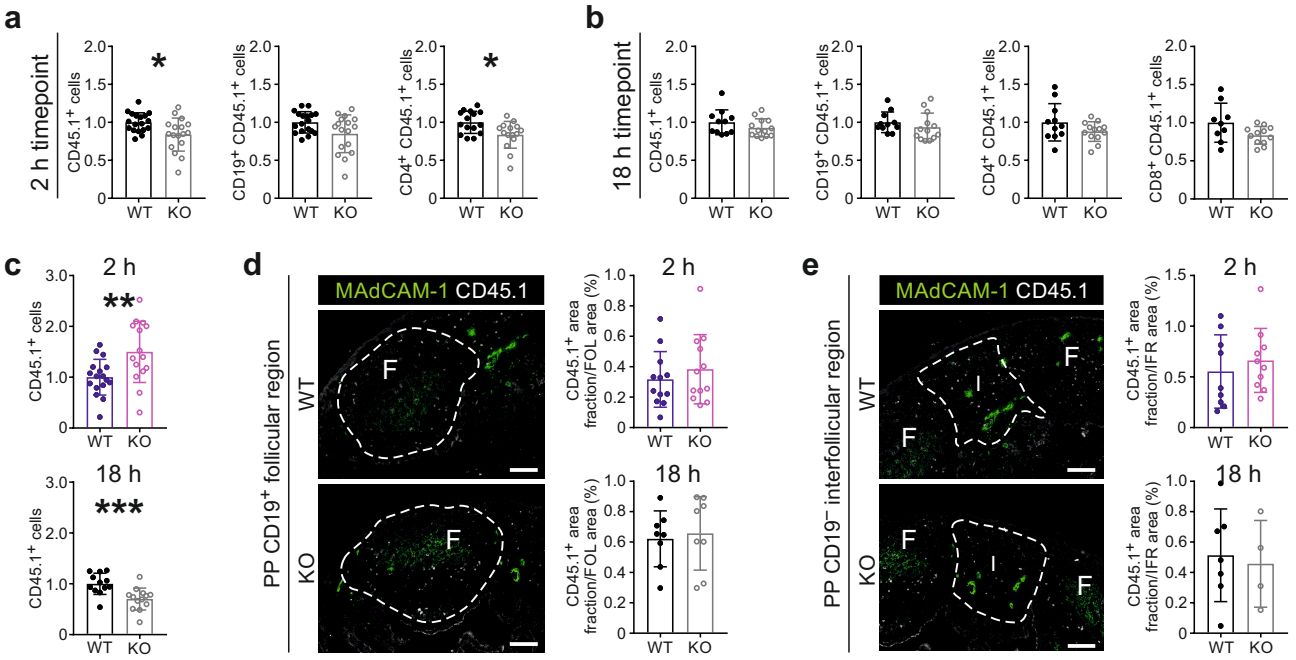
a
2 h timepoint
CD45.1+ cells
CD19+ CD45.1+ cells
CD4+ CD45.1+ cells
b
18 h timepoint
CD45.1+ cells
CD19+ CD45.1+ cells
CD4+ CD45.1+ cells
CD8+ CD45.1+ cells
WT
KO
c
2 h
18 h
CD45.1+ cells
d
PP CD19+ follicular region
MAdCAM-1 CD45.1
F
CD45.1+ area fraction/FOL area (%)
e
PP CD19− interfollicular region
I
CD45.1+ area fraction/IFR area (%)

Figure 4

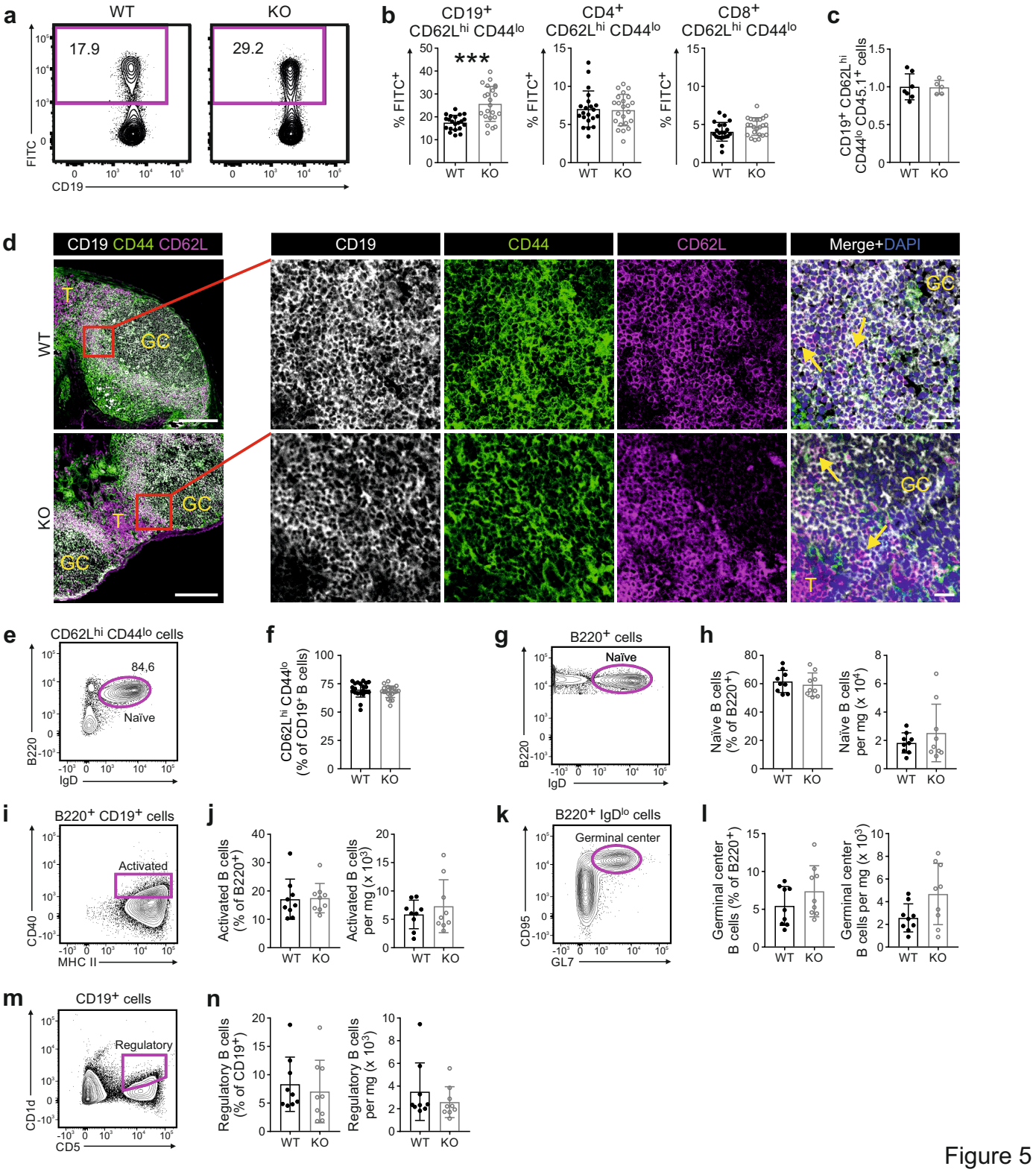
a
WT
KO
17.9
29.2
FITC
CD19
b
CD19+ CD62Lhi CD44lo
CD4+ CD62Lhi CD44lo
CD8+ CD62Lhi CD44lo
% FITC+
***
WT
KO
c
CD19+ CD62Lhi CD44lo CD45.1+ cells
d
CD19 CD44 CD62L
CD19
CD44
CD62L
Merge+DAPI
WT
KO
T
GC
e
CD62Lhi CD44lo cells
84,6
Naïve
B220
IgD
f
CD62Lhi CD44lo (% of CD19+ B cells)
g
B220+ cells
Naïve
h
Naïve B cells (% of B220+)
Naïve B cells per mg (x 10^4)
i
B220+ CD19+ cells
Activated
CD40
MHC II
j
Activated B cells (% of B220+)
Activated B cells per mg (x 10^3)
k
B220+ IgDlo cells
Germinal center
CD95
GL7
l
Germinal center B cells (% of B220+)
Germinal center B cells per mg (x 10^3)
m
CD19+ cells
Regulatory
CD1d
CD5
n
Regulatory B cells (% of CD19+)
Regulatory B cells per mg (x 10^3)

Figure 5

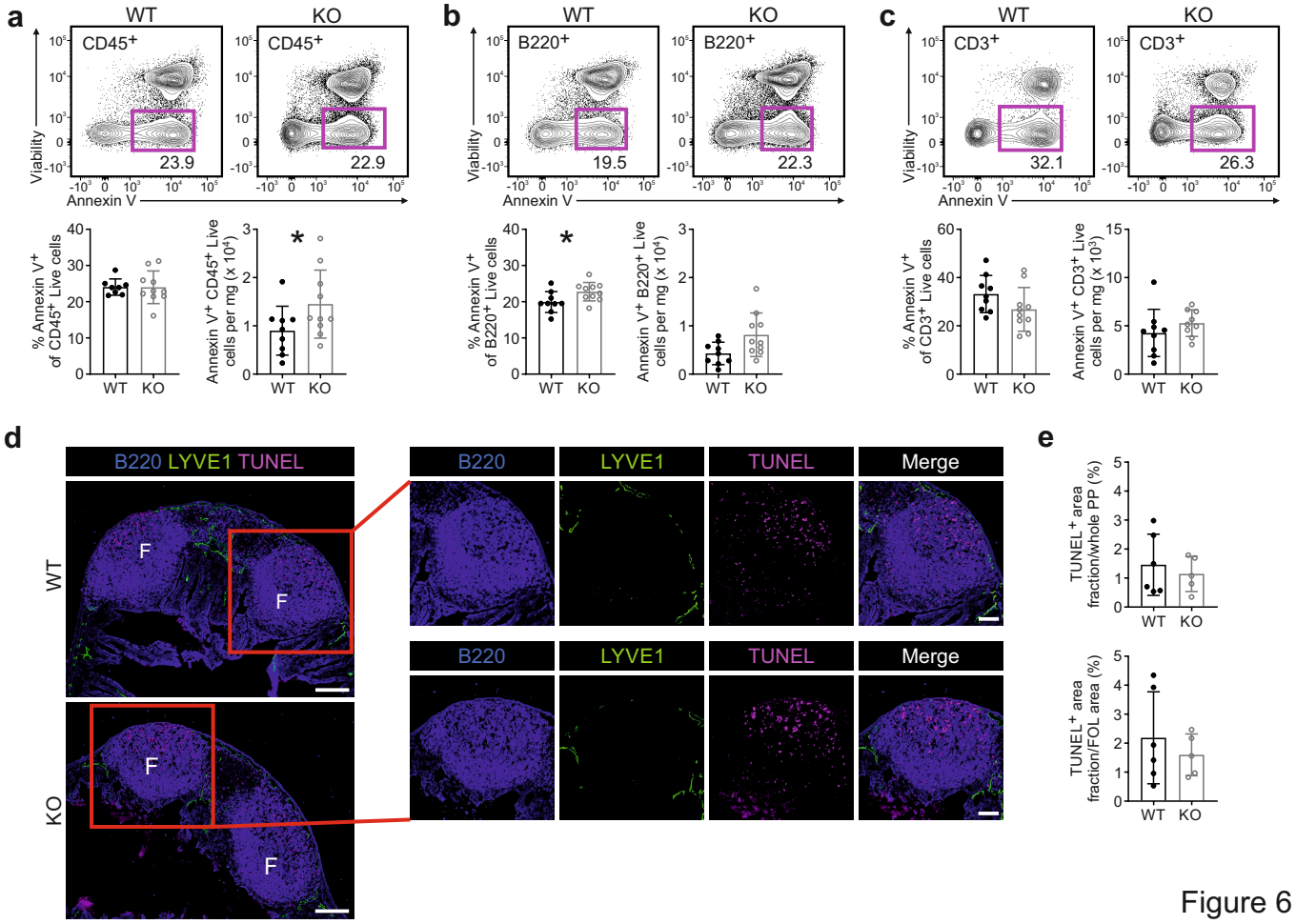
a
WT
KO
CD45+
23.9
22.9
Viability
Annexin V
% Annexin V+ of CD45+ Live cells
Annexin V+ CD45+ Live cells per mg (x 10⁴)
b
B220+
19.5
22.3
% Annexin V+ of B220+ Live cells
Annexin V+ B220+ Live cells per mg (x 10⁴)
c
CD3+
32.1
26.3
% Annexin V+ of CD3+ Live cells
Annexin V+ CD3+ Live cells per mg (x 10³)
d
B220 LYVE1 TUNEL
B220
LYVE1
TUNEL
Merge
F
e
TUNEL+ area fraction/whole PP (%)
TUNEL+ area fraction/FOL area (%)

Figure 6

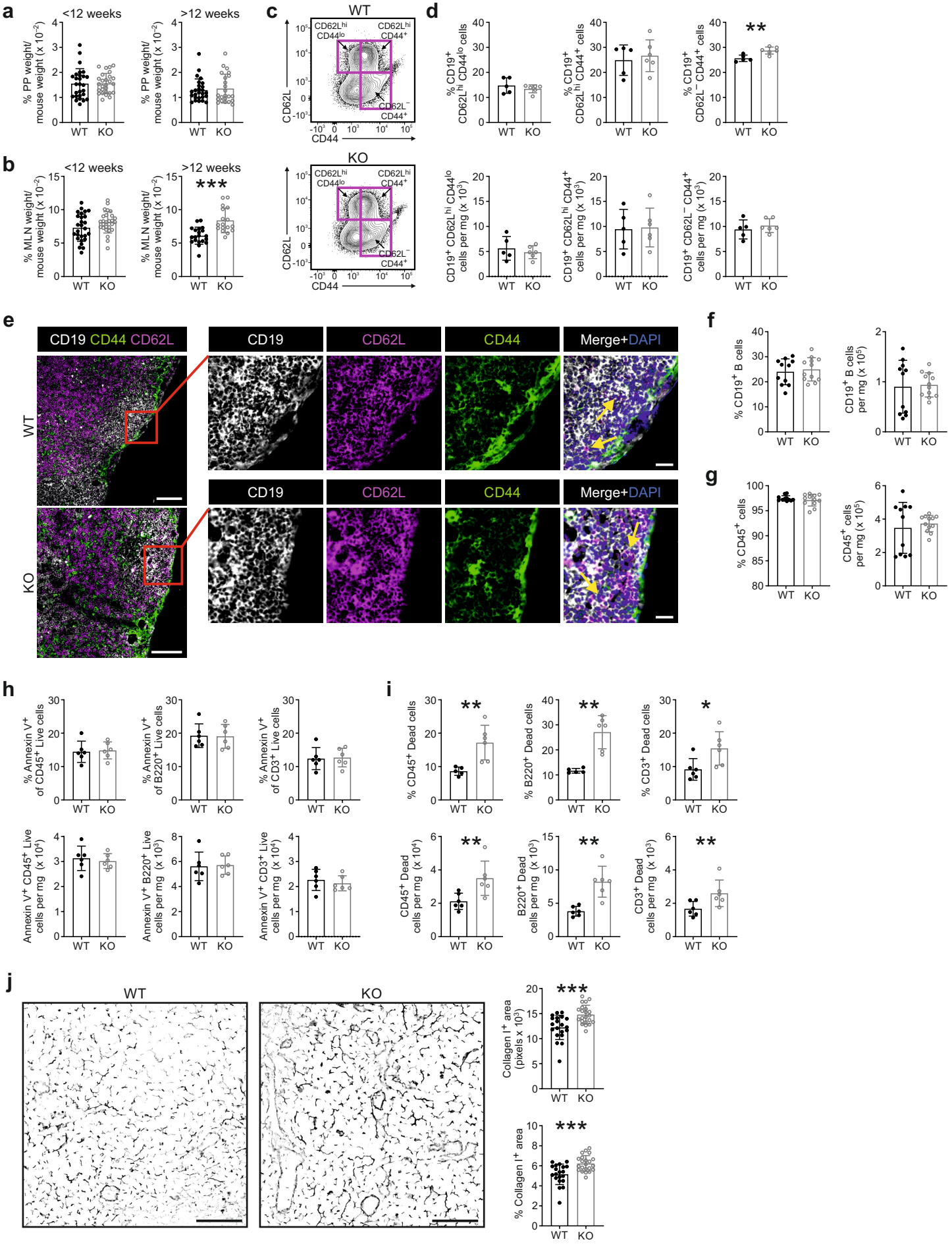
a
<12 weeks
>12 weeks
% PP weight/ mouse weight (x 10⁻²)
WT
KO
b
% MLN weight/ mouse weight (x 10⁻²)
***
c
WT
KO
CD62L^hi CD44^lo
CD62L^hi CD44^+
CD62L^− CD44^+
CD62L
CD44
d
% CD19^+ CD62L^hi CD44^lo cells
% CD19^+ CD62L^hi CD44^+ cells
% CD19^+ CD62L^− CD44^+ cells
**
CD19^+ CD62L^hi CD44^lo cells per mg (x 10³)
CD19^+ CD62L^hi CD44^+ cells per mg (x 10³)
CD19^+ CD62L^− CD44^+ cells per mg (x 10³)
e
CD19 CD44 CD62L
CD19
CD62L
CD44
Merge+DAPI
WT
KO
f
% CD19^+ B cells
CD19^+ B cells per mg (x 10⁵)
g
% CD45^+ cells
CD45^+ cells per mg (x 10⁵)
h
% Annexin V^+ of CD45^+ Live cells
% Annexin V^+ of B220^+ Live cells
% Annexin V^+ of CD3^+ Live cells
Annexin V^+ CD45^+ Live cells per mg (x 10⁴)
Annexin V^+ B220^+ Live cells per mg (x 10³)
Annexin V^+ CD3^+ Live cells per mg (x 10⁴)
i
% CD45^+ Dead cells
% B220^+ Dead cells
% CD3^+ Dead cells
CD45^+ Dead cells per mg (x 10⁴)
B220^+ Dead cells per mg (x 10³)
CD3^+ Dead cells per mg (x 10³)
j
WT
KO
Collagen I^+ area (pixels x 10⁵)
% Collagen I^+ area

Figure 7

Supplementary Methods

Production of anti-Robo4 monoclonal antibody

A Robo4 KO mouse was immunized with 5 µg of recombinant Robo4 (MBS2546674) in Freund's incomplete adjuvant by s.c. injections of the mixture into the footpad once a week for three weeks. The draining popliteal lymph node was harvested, lymphocytes were mechanically extracted from the tissue and fusion of lymphocytes to the myeloma cell line SP2/0 and hybridoma cell line production was performed with the ClonaCell™-HY Hybridoma Kit (Stemcell Technologies, 03800) according to the manufacturer's instructions. Hybridoma cell lines were cultured in Dulbecco's modified eagle medium (Sigma, D6429) during clone selection and positive clones were adapted to CD Hybridoma medium (Gibco, 11279-023). CD medium was exchanged into PBS using 100-kDa cutoff centrifugal filter units (Millipore, UCF910024) and the monoclonal antibody was stored at +4 °C. Isotypes for monoclonal antibodies were detected using the Pierce™ Rapid Antibody Isotyping Kit plus Kappa and Lambda - Mouse (Thermo Scientific, 26179) according to manufacturer's instructions.

Validation of monoclonal antibody

Hek-EBNA transfections. Hek-EBNA cells (hereafter referred to as Hek cells) were cultured in Dulbecco's modified eagle medium (Sigma, D6429) supplemented with 10% fetal calf serum, penicillin/streptomycin and geneticin 0,25 mg/ml. Cells at passage 6-10 were transfected with a commercially available murine Robo4-myc plasmid (Sino Biological, MG51081-CM) with Lipofectamine™ 2000 Transfection Reagent (Invitrogen™, 11668-030).

Flow cytometry. Transfected Hek-mRobo4-myc cells and Hek cells were blocked with 2% normal human AB serum and stained with hybridoma supernatants or the isotype control Ak1 (mouse IgG1) for Robo4-positive

clone validation. Surface stainings were performed as described in the Materials and methods section. Primary antibodies were detected with a donkey anti-mouse IgG (H+L) Alexa Fluor 647 secondary antibody (Invitrogen™, A31571). Commercially available rat anti-mouse Robo4-PE (R&D, FAB50041P) and its isotype control rat IgG2a-PE (R&D, IC006P) were used as positive controls. For intracellular staining, the cells were fixed and permeabilized by incubating them in ice-cold methanol for 10 min at -20 °C before staining with antibodies. Samples were run with an LSR Fortessa cytometer (Becton Dickinson).

Immunofluorescence. Transfected Hek-mRobo4-myc cells were cytospinned onto microscopic slides and fixed with acetone or methanol. Cells were incubated with hybridoma supernatants or without the primary antibody in the negative control. Robo4-detecting positive clones were detected with a goat anti-mouse IgG (H+L) Alexa Fluor 546 secondary antibody (Invitrogen™, A11030) and samples were mounted using ProLong™ Gold Antifade Mountant with DAPI (Invitrogen™, P36931).

Enzyme-linked immunosorbent assay. Nunc MaxiSorp plates were coated with 1 µg of recombinant murine Robo4 (MBS2546674) in 0,1 M $NaHCO_3$ (pH 9.6) overnight at +4 °C and blocked with 1% BSA in PBS for 1h at room temperature. Supernatant containing monoclonal antibodies or positive controls diluted in PBS supplemented with 1% BSA and negative controls were added to wells followed by incubation of HRP-conjugated secondary antibodies, both 1h at room temperature. Robo4 reactive antibodies were visualized by adding TMB chromogen (Invitrogen) and reactions were stopped with 0,1 M HCl after approximately 2 minutes. Absorbance was measured using Tecan Infinite M200 and analyzed with the Magellan software (Tecan).

Quantitative PCR for B cells

PPs were harvested from Robo4 KO and WT mice and homogenized to produce single-cell suspensions as described under Flow Cytometry. B cells were selected using the B Cell Isolation Kit (Miltenyi Biotec, 130-090-862) according to the manufacturer's instructions. Selection was verified with FACS staining. Total RNA was isolated from the sorted cells using the NucleoSpin RNA Kit (Macherey Nagel). The RNA was subsequently reverse transcribed to cDNA with SuperScript VILO cDNA Synthesis Kit (Invitrogen) according to the manufacturer's instructions. Quantitative PCR was carried out using TaqMan Universal Master Mix II (Thermo Fisher Scientific) with probes and primers designed with the Universal Probe Library Assay Design Center (RocheLifeScience) for *Cxcr4, Cxcr5, S1pr1,* and *Actb* (Supplementary Table 2). The reactions were run using the Applied Biosystems' Quant Studio 3 Real-Time PCR System (Thermo Fisher Scientific). Relative expression levels were calculated using Applied Biosytems® analysis modules in Thermo Fisher Cloud computing platform (ThermoFisher Scientific). The results were presented as percentages of control gene mRNA levels from the same sample.

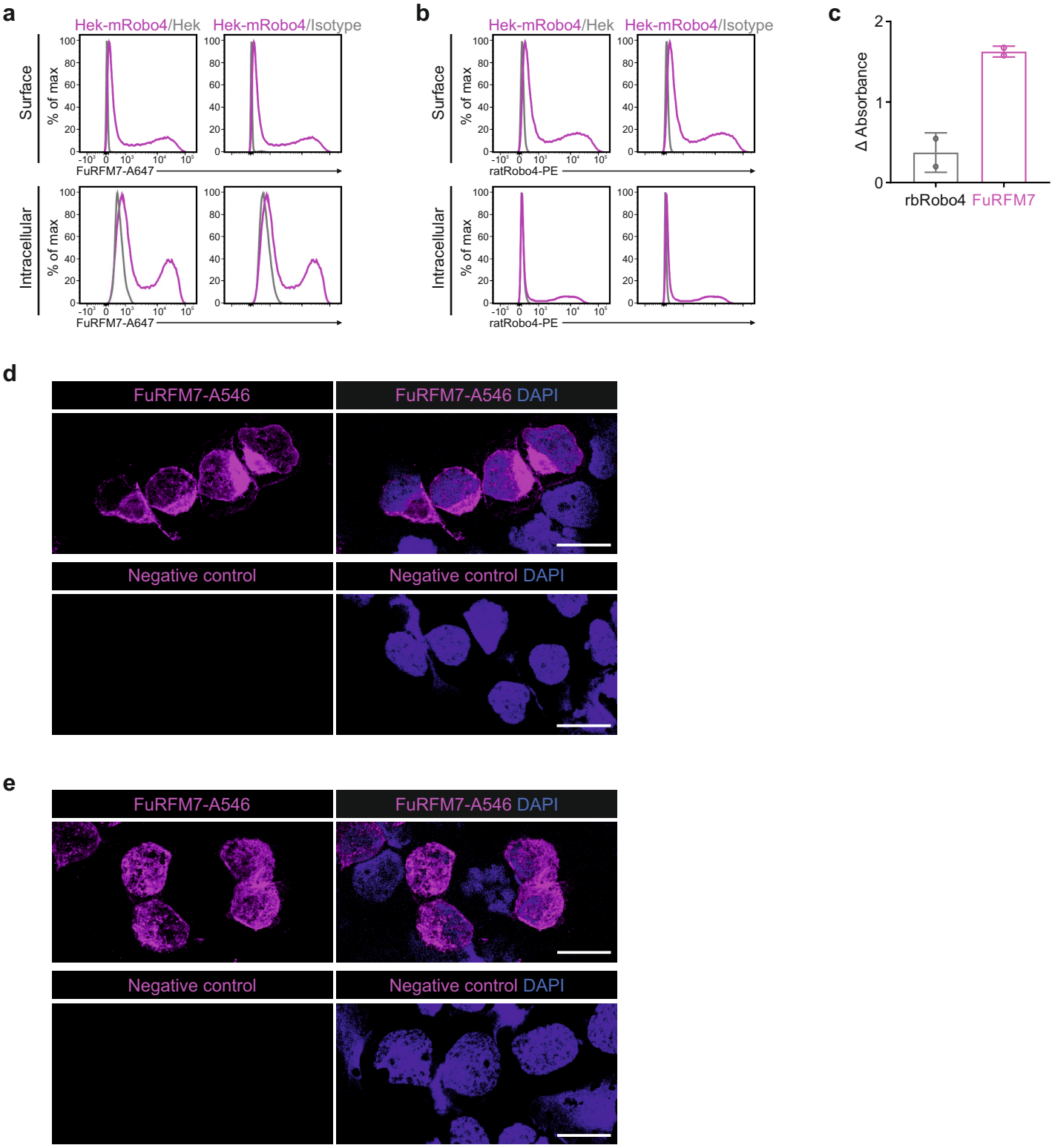

Supplementary Figure 1 Monoclonal anti-Robo4 antibody validation. **a, b** Surface and intracellular FACS staining showing Robo4-positivity in Hek-mRobo4-myc cells and native Hek cells stained with FuRFM7 (**a**) as well as commercially available rat anti-mouse Robo4-PE (**b**). Magenta histograms, Robo4 staining, grey histograms, negative control of non-transfected Hek cells or isotype controls, n=3. **c** Robo4 protein was detected with ELISA using clone FuRFM7 or commercially available rabbit anti-mouse Robo4, n=2. **d, e** Immunofluorescence staining of cytospinned Hek-mRobo4-myc cells with FuRFM7 after fixing with acetone (**d**) or methanol (**e**). The primary antibody was omitted from the negative control staining. Scale bars 20 µm, n=1 in **d** and **e**.

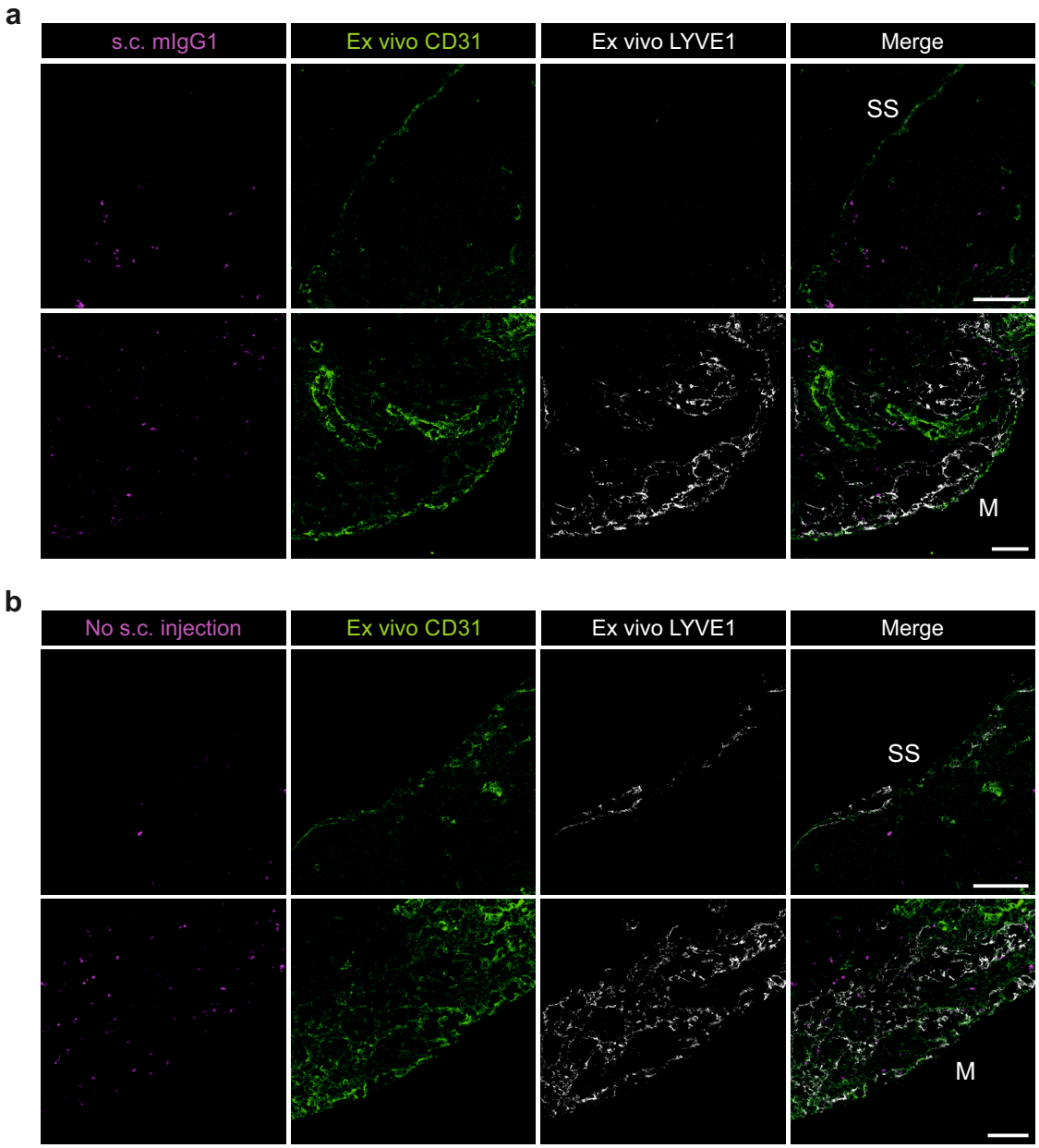

Supplementary Figure 2 Negative controls for subcutaneously injected anti-Robo4 antibody, clone FuRFM7. **a** Subcutaneous (s.c.) injections of a conjugated isotype control, mouse IgG1-A647 after *in vivo* blocking with anti-CD16/CD32 antibody and mouse immunoglobulins. **b** An untouched popliteal lymph node without any s.c. injections imaged with the same settings as in Fig. 1d and SFig. 2a. Samples were stained *ex vivo* with endothelial markers CD31 and LYVE1. Scale bars 50 µm, n=3. SS, subcapsular sinus, M, medullary sinus.

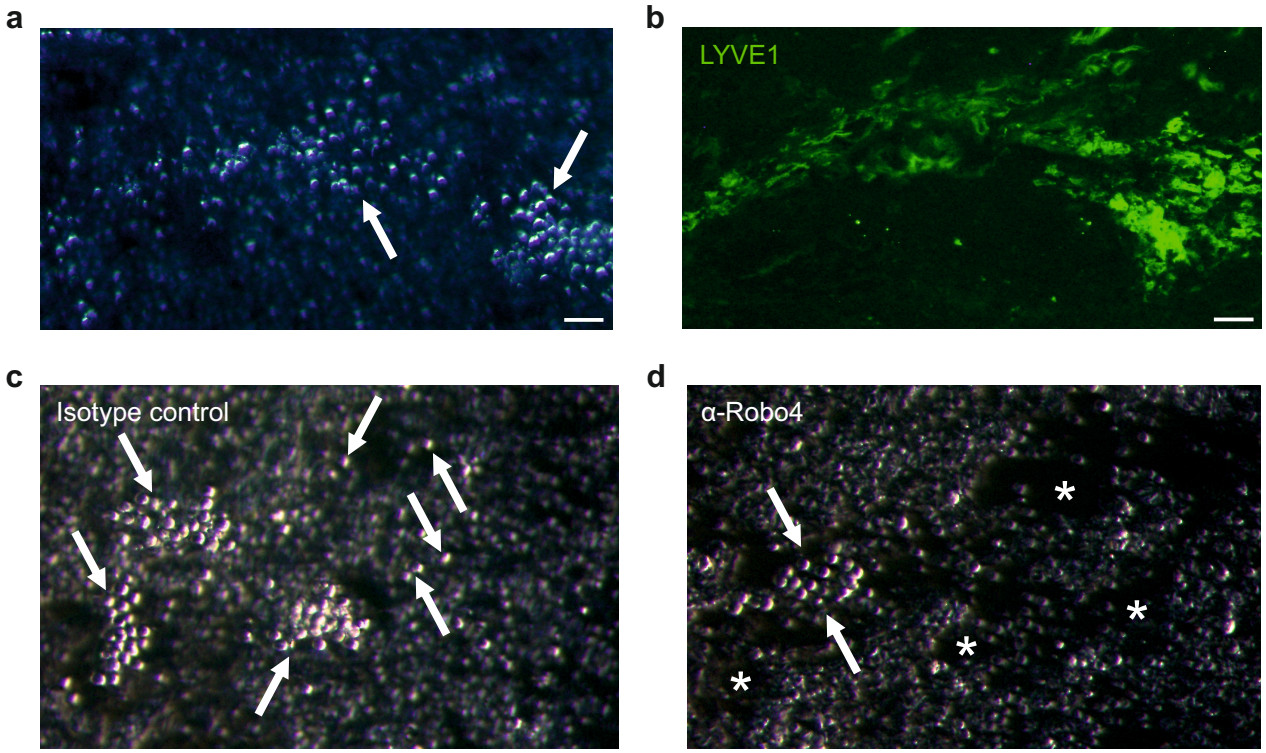

Supplementary Figure 3 Examples of *ex vivo* adhesion assay. **a, b** In this assay lymphocytes bind to LYVE1 positive lymphatics (green in **b**) in a human peripheral lymph node. Staining with anti-LYVE1 antibody is performed on a separate section as glutaraldehyde fixing (see materials and methods) of the bound lymphocytes prevents the recognition of LYVE1. **c** Lymphocyte binding to lymphatic sinuses in the presence of the control antibody. **d** Binding to the same lymphatic sinus network but on a different section in the presence of the anti-Robo4 antibody. In **c** and **d** arrows indicate lymphocytes that have adhered to lymphatic sinuses, whereas asterisks in **d** mark empty lymphatic sinuses. The focus of the picture is always a compromise as the bound lymphocytes are on a different level than the frozen lymph node section. Scale bars 50 µm.

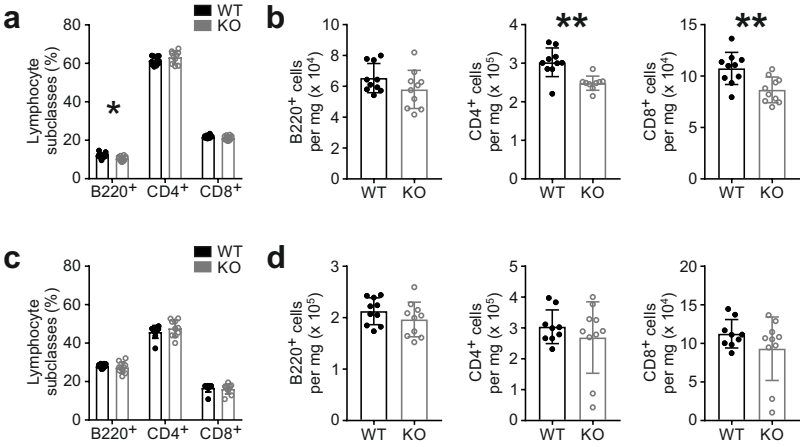

Supplementary Figure 4 Endogenous B and T cells in Robo4 KO and WT animals. Frequency (**a, c**) and number (**b, d**) of B220, CD4 and CD8 positive cells in PLN (**a, b**) and MLN (**c, d**)**.** Each dot represents one mouse. Data are presented as mean ± SD, * $P < 0.05$, ** $P < 0.01$ (Mann-Whitney *U*-test).

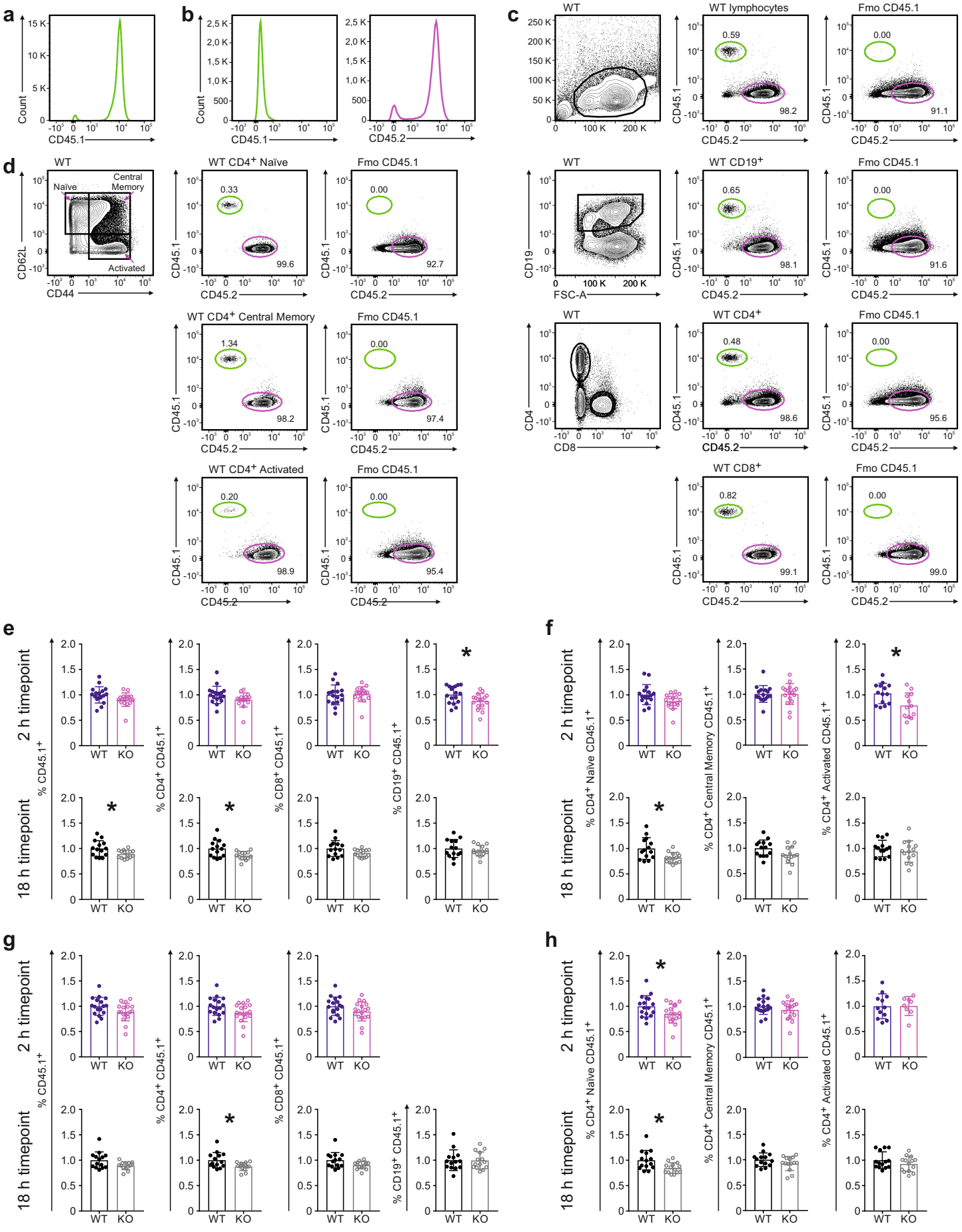
a
b
c
d
e
f
g
h
Count
CD45.1
CD45.2
WT
WT lymphocytes
Fmo CD45.1
WT CD4+ Naïve
WT CD19+
WT CD4+
WT CD8+
WT CD4+ Central Memory
WT CD4+ Activated
Naïve
Central Memory
Activated
CD62L
CD44
CD19
FSC-A
CD4
CD8
0.59
98.2
0.00
91.1
0.33
99.6
92.7
0.65
98.1
91.6
0.48
98.6
95.6
1.34
98.2
97.4
0.20
98.9
95.4
0.82
99.1
99.0
2 h timepoint
18 h timepoint
% CD45.1+
% CD4+ CD45.1+
% CD8+ CD45.1+
% CD19+ CD45.1+
% CD4+ Naïve CD45.1+
% CD4+ Central Memory CD45.1+
% CD4+ Activated CD45.1+
WT
KO

Supplementary Figure 5 Minor but statistically significant differences in the homing of adoptively transferred lymphocytes to MLN and PLN in Robo4 KO and their WT controls. **a** Adoptively transferred lymphocytes were isolated from CD45.1$^+$ donors. **b** Robo4 KO and WT recipient mice carry the CD45.2 allele for CD45. **c, d** Representative images for gating the flow cytometry data. **c** Lymphocytes were gated based on FSC/SSC plots after removal of duplicate cells, and further gated for CD19$^+$ B cells, CD4$^+$ and CD8$^+$ T cells. The percentage of CD45.1$^+$ adoptively transferred and CD45.2$^+$ endogenous cells were gated from total lymphocytes and the B and T cell gates. **d** CD4$^+$ T cells were further gated on naïve (CD62L$^+$ CD44$^-$), central memory (CD62L$^+$ CD44$^+$) and activated (CD62L$^-$ CD44$^+$) subpopulations, and the percentage of transferred CD45.1$^+$ was examined from the CD4$^+$ subpopulations. Fmo (fluorescence minus one) staining of a WT recipient mouse, which did not receive adoptively transferred cells, was used to gate the CD45.1$^+$ population. **e-h** Relative amount of adoptively transferred CD45.1$^+$ lymphocytes, CD4$^+$ CD45.1$^+$ and CD8$^+$ CD45.1$^+$ T cells as well as CD19$^+$ CD45.1$^+$ B cells recovered in MLN (**e**) and PLN (**g**) at 2 hours (top) or 18 hours (bottom) after intravenous injections of donor cells into Robo4 KO and WT recipients. Relative amount of adoptively transferred CD4$^+$ CD45.1$^+$ T cell subpopulations recovered from MLN (**f**) and PLN (**h**) at 2 hours (top) or 18 hours (bottom) after intravenous injections of donor cells into Robo4 KO and WT recipients. Data are pooled from three independent 2-hour and two independent 18-hour adoptive transfer assays with 8-18 KO, 12-17 WT mice (2 hours) and 14 KO, 13-14 WT mice (18 hours). Each dot represents an individual mouse. Data are presented as mean ± S.D. * $P < 0.05$ (Mann-Whitney *U*-test).

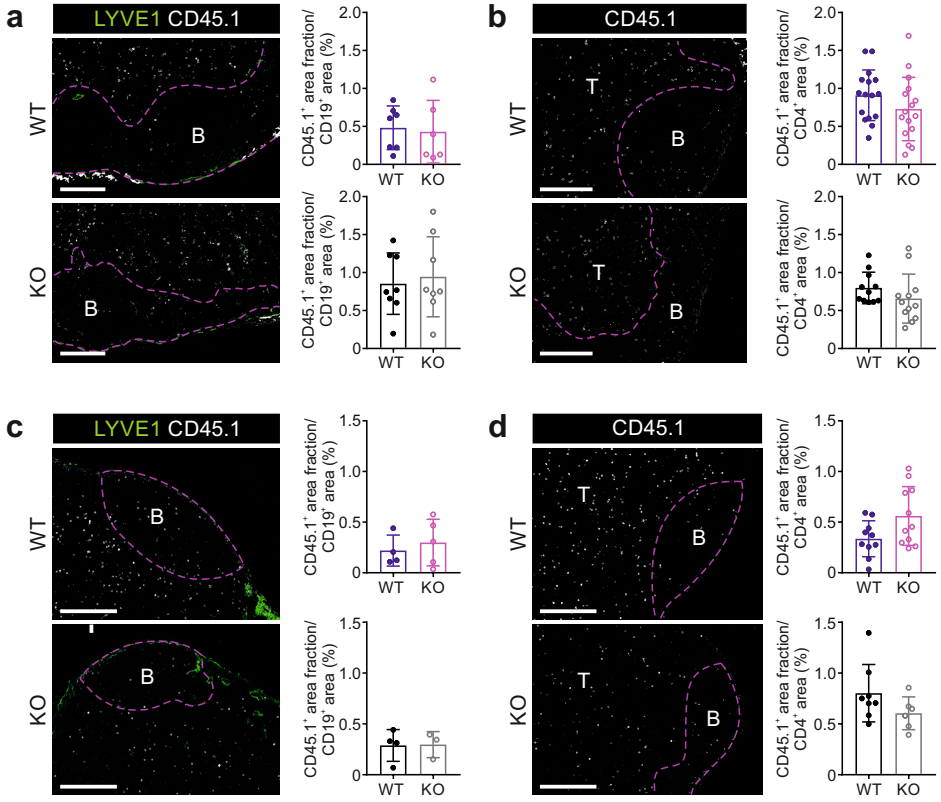

Supplementary Figure 6 Intra-organ distribution of adoptively transferred lymphocytes in PLN and MLN of Robo4 KO and WT mice. **a-d** Image analysis of adoptively transferred CD45.1$^+$ cells from CD19$^+$ B cell areas (**a, c**) and CD4$^+$ T cell areas (**b, d**) quantified from mesenteric lymph nodes (**a, b**) or peripheral lymph nodes (**c, d**) 2 hours (top graph) or 18 hours (bottom graph) after intravenous injections. In each case the percentage of the area of CD45.1$^+$ cells was calculated from the depicted B cell or T cell areas. For MLN samples, an area of 1.61-1.62 mm^2 was selected as a representative area for the tissue. For each sample, 1-2 representative areas were quantified. Data from the 2-hour adoptive transfer experiment are quantified from 1-2 independent experiments. MLN samples were analyzed from 4 KO and 4 WT mice, 1-2 sections and 1-2 representative areas/tissue. PLN samples were analyzed from 5-7 KO and 4-6 WT mice, 1-2 sections/mouse. Data from the 18-hour adoptive transfer experiment are presented from one independent experiment. MLN samples were analyzed from 3-4 WT and KO mice, 1-2 sections/sample and 1-2 representative areas/tissue. PLN samples were analyzed from 4 WT and 3 KO mice, 1-2 sections/mouse. Each dot represents a single analyzed area (MLN) or section (PLN). Data are presented as mean ± S.D.

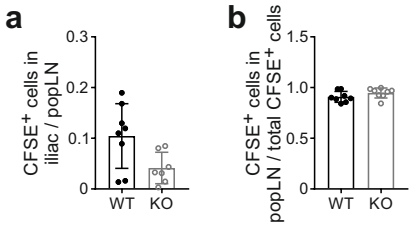

Supplementary Figure 7 Lymphocytes tend to have poorer exit form PLN in Robo4 KO than in WT mice. **a, b** Adoptively transferred CFSE$^+$ cells assessed by flow cytometry from popliteal and iliac lymph nodes (LN) 12 hours after their adoptive transfer into the footpad of Robo4 KO and WT recipient mice. Results are presented as a ratio CFSE$^+$ cells recovered from the iliac LN in relation to cells recovered from the popliteal LN (**a**)**,** and as CFSE$^+$ cells recovered from the popliteal LN in relation to the total amount of CFSE$^+$ cells recovered from the popliteal and iliac LNs (**b**). Data are presented as mean ± S.D. and are from one experiment analyzed from 7-8 independent lymph nodes collected from 5 KO and 5 WT mice.

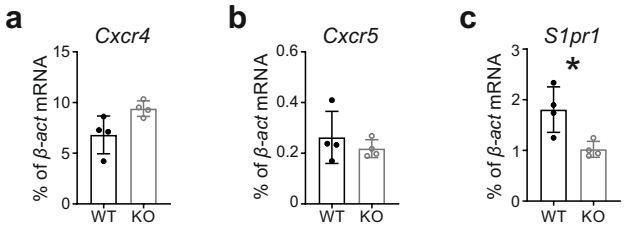

Supplementary Figure 8 Expression of lymphocyte egress related genes in Robo4 KO B cells. **a-c** The expression of *Cxcr4* (**a**), *Cxcr5* (**b**) and *S1pr1* (**c**) was analyzed with quantitative PCR from B cells isolated from Robo4 KO and WT PPs. Each dot represents an individual mouse. Data are presented as mean ± S.D. and were analyzed from 4 KO and 4 WT mice. * $P < 0.05$ (Mann-Whitney *U*-test).

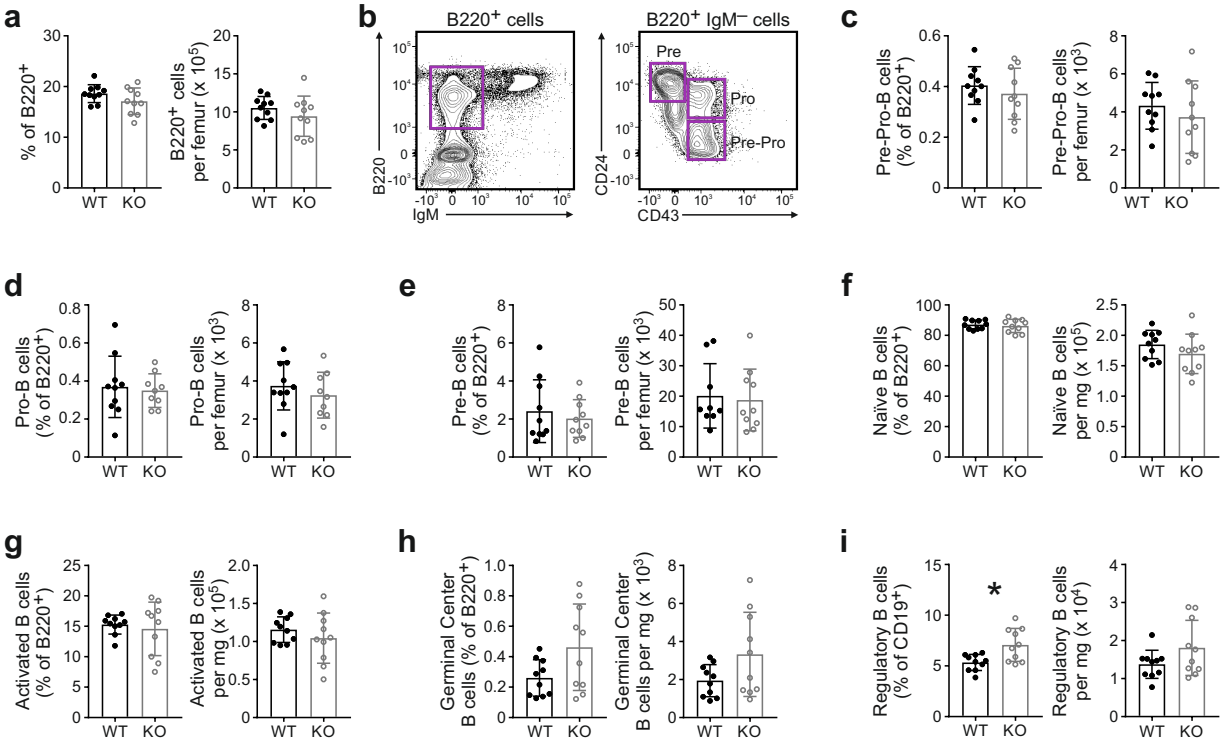

Supplementary Figure 9 B cell populations analyzed from Robo4 KO and WT bone marrow and MLN are comparable except for regulatory B cells of the MLN. **a** Frequency (%) and cell number of B220$^+$ B cells in the bone marrow of Robo4 KO and WT femurs assessed by flow cytometry. **b-e** B cell progenitors analyzed from the bone marrow of Robo4 KO and WT mice. **b** Gating strategy for analyzing bone marrow B cell progenitors. Quantification of Pre-Pro B cells (B220$^+$ IgM$^-$ CD24$^-$ CD43$^+$, **c**), Pro-B cells (B220$^+$ IgM$^-$ CD24$^+$ CD43$^+$, **d**) and Pre-B cells (B220$^+$ IgM$^-$ CD24$^+$ CD43$^-$, **e**) presented as percentage of B220$^+$ B cells as well as total cell numbers recovered from the femur of Robo4 KO and WT mice. **f-i** Analysis of endogenous B cell subpopulations in Robo4 KO and WT mesenteric lymph nodes (MLN). Quantification of naïve B cells (B220$^+$ IgD$^+$, **f**), activated B cells (B220$^+$ CD19$^+$ CD40$^+$ MHCII$^+$, **g**), germinal center B cells (B220$^+$ IgD^{lo} CD95$^+$ GL7$^+$, **h**) and regulatory B cells (CD19$^+$ CD1d$^+$ CD5$^+$, **i**) presented as percentage of B220$^+$ B cells as well as total cell numbers per mg of tissue. Representative FACS gating is shown in Fig. 5. Data are pooled from two independent experiments performed with 10 WT and 10 KO mice. * $P < 0.05$ (Mann-Whitney U-test).

Supplementary Table 1

Antibody[a]	Clone	Cat	Company[b]	Concentration	Application[c]
Primary antibodies					
Rabbit anti-mouse Collagen Type I	pAb	AB765P	Millipore	10 µg/ml	IF
Rabbit anti-mouse LYVE-1	pAb	103-PA50	ReliaTech GmbH	5 µg/ml	IF
Rat anti-mouse MAdCAM-1	Meca367	Ref [d]	In house	10 µg/mouse	i.v. Staining
Rat anti-mouse MAdCAM-1	Meca367	Ref [d]	In house	0,5 µg/ml	IF
Rat anti-mouse CD16/CD32	2.4G2	BE0307	Bio X Cell	-	In vivo blocking
Rat anti-mouse CD16/CD32 Mouse BD Fc block™	2.4G2	553141	BD Pharmingen™	75 µg/ml	Flow Cyt
Rat anti-mouse CD19	6D5	115502	BioLegend®	7 µg/ml	IF
Rat anti-mouse CD62L	MEL-14	Ref [e]	In house	10 µg/ml	IF
Mouse anti-mouse Robo4	FuRFM7	-	In house	Supernatant	Flow Cyt, IF, ELISA
Rabbit anti-mouse Robo4	pAb	bs-5795R	Bioss Antibodies	1 µg/ml	Western Blotting, ELISA
Rat anti-mouse Robo4	274940	MAB5004	R&D systems	10 µg/ml	Flow Cyt
Isotype controls					
Mouse IgG1, isotype control	Ak1	-	InVivo BioTech Services GmbH	10 µg/ml	Flow Cyt
Rat IgG2a-FITC, isotype control	R35-95	553929	BD Pharmingen™	1 µg/ml	Flow Cyt
Rat IgG2a-PE, isotype control	R35-95	553930	BD Pharmingen™	2 µg/ml	Flow Cyt
Rat IgG2a-PE, isotype control	54447	IC006P	R&D Systems	1/100	Flow Cyt
Secondary antibodies					
Donkey anti-goat IgG (H+L) Alexa Fluor® 488	pAb	A11055	Invitrogen™	5 µg/ml	IHC
Goat anti-mouse IgG Alexa Fluor® 488	pAb	A11029	Invitrogen™	5 µg/ml	IHC
Goat anti-rat IgG (H+L), Alexa Fluor® 488	pAb	A11006	Invitrogen™	5 µg/ml	IF
Goat anti-rat IgG (whole molecule)-FITC	pAb	G6258	Sigma-Aldrich	1/100	Flow Cyt
Goat anti-rabbit IgG (H+L) Alexa Fluor® 546	pAb	A11035	Invitrogen™	5 µg/ml	IF
Goat anti-rat IgG (H+L), Alexa Fluor® 546	pAb	A11081	Invitrogen™	5 µg/ml	IF
Streptavidin, Alexa Fluor™ 546 conjugate		S11225	Invitrogen™	0,5 µg/ml	IF
Donkey anti-goat IgG (H+L) Alexa Fluor® 633	pAb	A21082	Invitrogen™	5 µg/ml	IHC
Goat anti-rat IgG (H+L) Alexa Fluor® 647	pAb	A21247	Invitrogen™	5 µg/ml	IF
Donkey anti-mouse IgG (H+L) Alexa Fluor® 647	pAb	A31571	Invitrogen™	2 µg/ml	Flow Cyt
Rabbit anti-mouse immunoglobulins/HRP	pAb	P0260	Dako	6,5 µg/ml	ELISA
Swine anti-rabbit immunoglobulins/HRP	pAb	P0217	Dako	6,5 µg/ml	ELISA
Conjugated antibodies					
Annexin V-PE		556422	BD Pharmingen™	1:200	Flow Cyt
Fixable Viability Dye eFluor™ 506		65-0866-14	eBioscience™	1:1000	Flow Cyt
Rat anti-mouse CD1d-PerCP-Cy™5.5	1B1	562713	BD Pharmingen™	1 µg/ml	Flow Cyt
Rat anti-mouse CD3 Alexa Fluor® 647	17A2	557869	BD Pharmingen™	1 µg/ml	Flow Cyt
Rat anti-mouse CD4 Alexa Fluor® 647	RM4-5	557681	BD Pharmingen™	10 µg/ml	IF
Rat anti-mouse CD4-APC Cy™7	GK1.5	552051	BD Pharmingen™	1 µg/ml	Flow Cyt
Rat anti-mouse CD4-BV510	RM4-5	100553	BioLegend®	1 µg/ml	Flow Cyt
Rat anti-mouse CD5 PE	53-7.3	553023	BD Pharmingen™	1 µg/ml	Flow Cyt
Rat anti-mouse CD8a Alexa Fluor® 488	53-6.7	557668	BD Pharmingen™	10 µg/ml	IF
Rat anti-mouse CD8a-BV650	53-6.7	563234	BD Horizon™	1 µg/ml	Flow Cyt
Rat anti-mouse CD8a-BV711	53-6.7	100747	BioLegend®	1 µg/ml	Flow Cyt
Rat anti-mouse CD11b APC Cy™7	M1/70	561039	BD Pharmingen™	2 µg/ml	Flow Cyt
Rat anti-mouse CD19 Alexa Fluor® 647	6D5	115522	BioLegend®	10 µg/ml	IF
Rat anti-mouse CD19-APC Cy™7	1D3	557655	BD Pharmingen™	1 µg/ml	Flow Cyt
Rat anti-mouse CD19-BV421	6D5	115537	BioLegend®	0,5 µg/ml	Flow Cyt
Rat anti-mouse CD19-BV510	1D3	562956	BD Horizon™	1 µg/ml	Flow Cyt
Rat anti-mouse CD24 BV650	M1/69	563545	BD Horizon™	1 µg/ml	Flow Cyt
Rat anti-mouse CD31 Alexa Fluor® 488	MEC13.3	102514	BioLegend®	7 µg/ml	IF
Rat anti-mouse CD31-APC	MEC13.3	102510	BioLegend®	2 µg/ml	Flow Cyt
Rat anti-mouse CD40 PE-CF594	3/23	562847	BD Horizon™	1 µg/ml	Flow Cyt
Rat anti-mouse CD43-BV605	S7	563205	BD Horizon™	1 µg/ml	Flow Cyt
Rat anti-mouse CD44 APC	IM7	17-0441-82	eBioscience™	1 µg/ml	Flow Cyt
Rat anti-mouse CD44 FITC	IM7	553133	BD Pharmingen™	10 µg/ml	IF
Rat anti-mouse CD44 PerCP-Cy™5.5	IM7	560570	BD Pharmingen™	1 µg/ml	Flow Cyt
Rat anti-mouse CD45 PE	30-F11	553081	BD Pharmingen™	1 µg/ml	Flow Cyt
Rat anti-mouse CD45 APC-Cy™7	30-F11	557659	BD Pharmingen™	2 µg/ml	Flow Cyt
Rat anti-mouse CD45 FITC	30-F11	553079	BD Pharmingen™	2,5 µg/ml	Flow Cyt
Mouse anti-mouse CD45.1 FITC	A20	553775	BD Pharmingen™	2,5 µg/ml	Flow Cyt
Mouse anti-mouse CD45.1 biotin	A20	110704	BioLegend®	10 µg/ml	IF
Mouse anti-mouse CD45.2 APC	104	558702	BD Pharmingen™	1 µg/ml	Flow Cyt
Rat anti-mouse CD45R/B220 BV421	RA3-6B2	562922	BD Horizon™	0,5 µg/ml	Flow Cyt
Rat anti-mouse CD45R/B220 Pacific Blue™	RA3-6B2	558108	BD Pharmingen™	10 µg/ml	IF
Rat anti-human/mouse CD45R (B220) eFluor® 570	RA3-6B2	41-0452-80	eBioscience™	4 µg/ml	IF
Rat anti-mouse CD62L BV421	MEL-14	104436	BioLegend®	0,5 µg/ml	Flow Cyt
Rat anti-mouse CD62L Alexa Fluor® 647	MEL-14	104417	BioLegend®	1 µg/ml	Flow Cyt
Hamster anti-mouse CD95 PE	Jo2	554258	BD Pharmingen™	1 µg/ml	Flow Cyt
Rat anti-mouse IgD Alexa Fluor® 647	11-26c.2a	405708	BioLegend®	10 µg/ml	IF
Rat anti-mouse IgD BV786	11-26c.2a	563618	BD Horizon™	1 µg/ml	Flow Cyt
Rat anti-mouse IgM APC-eFluor 780	II/41	47-5790-80	eBioscience™	1 µg/ml	Flow Cyt
Rat anti-mouse LYVE1 Alexa Fluor® 488	ALY7	53-0443-82	eBioscience™	5-7 µg/ml	IF
Rat anti-mouse LYVE1 PE	223322	FAB2125P	R&D systems	5 µg/ml	Flow Cyt
Rat anti-mouse MHC II PE-Cy7	I-A/I-E	25-5321-82	eBioscience™	0,5 µg/ml	Flow Cyt
Hamster anti-mouse Podoplanin PE-Cy7	8.1.1	127412	BioLegend®	2 µg/ml	Flow Cyt
Mouse anti-mouse Robo4-A647	FuRFM7	-	In house	5 µg	s.c. Injection
Rat anti-mouse Robo4-PE	274914	FAB50041P	R&D systems	1/100	Flow Cyt
Rat anti-mouse T- and B-cell activation antigen Alexa Fluor® 647	GL7	561529	BD Pharmingen™	1 µg/ml	Flow Cyt
Human antibodies					
Mouse anti-human Clever-1	3-372	Ref [f]	In house	10 µg/ml	IHC
Rabbit anti-human Lyve-1	pAb	102-PA50AG	ReliaTech GmbH	10 µg/ml	IHC
Goat anti-human Prox-1	pAb	AF2727	R&D systems	10 µg/ml	IHC
Rabbit anti-human Robo4	pAb	NB110-58780	Novus Biologicals	5 µg/ml	IHC
Rabbit anti-human Robo4	pAb	ab10547	Abcam	10 µg/ml	In vitro adhesion assay

All primary antibodies had isotype matched control antibodies or normal serum/Ig from an appropriate animal

a) APC, Allophycocyanin; APC-Cy7, Allophycocyanin-indotricarbocyanine; BV421, Brilliant Biolet 421, BV510, Brilliant Violet 510; BV605, Brilliant Violet 605; BV650, Brilliant Violet 650; BV711, Brilliant Violet 711; BV786, Brilliant Violet 786; FITC, Fluorescein isothiocyanate; PE, Phycoerythrin; PE-CF594, Phycoerythrin-CF594; PE-Cy7, Phycoerythrin-Cyanine 7; PerCp-Cy5.5, Peridinin chlorophyll protein-cyanine 5.5
b) BD, Becton-Dickinson
c) IF, immunofluorescence; Flow Cyt, Flow Cytometry; IHC, immunohistochemistry
d) Nature 331:41 (1988)
e) Nature 304:30 (1983)
f) European Journal of Immunology 33:3 (2003)

Supplementary Table 2

Gene	Primer	Sequence	Probe
Actb	Left	ctaaggccaaccgtgaaaag	64
	Right	accagaggcatacagggaca	
Cxcr4	Left	tggaaccgatcagtgtgagt	38
	Right	gggcaggaagatcctattga	
Cxcr5	Left	gaatgacgacagaggttcctg	13
	Right	gcccaggttggcttcttat	
S1pr1	Left	cggtgtagacccagagtcct	66
	Right	agcttttccttggctggag	